THE FEASIBILITY OF HIGH RESOLUTION, THREE-DIMENSIONAL RECONSTRUCTION OF METAL-COATED SURFACES IN STRUCTURAL BIOLOGY

Jeremy David Woodward

A minithesis submitted in partial fulfilment of the requirements for the degree of
Magister Scientiae (Structural Biology) in the
Department of Biotechnology, University of the Western Cape
and
Electron Microscope Unit, University of Cape Town

Supervisor:

Associate Professor Bryan Trevor Sewell

November 2006

The financial assistance of the National Research Foundation (NRF) towards this research is hereby acknowledged. Opinions expressed and conclusions arrived at, are those of the author and are not necessarily to be attributed to the NRF.

KEYWORDS

Structural cell biology

Field emission transmission electron microscopy

Field emission scanning electron microscopy

Metal-shadowing

Macromolecules

3D reconstruction

Image Processing

Photogrammetry

Stereoscopy

Docking

ABSTRACT

The feasibility of high-resolution, three-dimensional reconstruction of metal-coated surfaces in structural biology

Jeremy David Woodward

MSc minithesis, Department of Biotechnology, University of the Western Cape and Electron Microscope Unit, University of Cape Town

Life is an emergent property of a complex network of interacting cellular-machines. Three-dimensional (3D), cellular structure captured at supra-atomic resolution has the potential to revolutionise our understanding of the interactions, dynamics and structure of these machines: proteins, organelles and other cellular constituents, in their normal functional states. Techniques, capable of acquiring 3D cellular structure at sufficient resolution to enable identification and interpretation of individual macromolecules in the cellular milieu, have the potential to provide this data.

Advances in cryo-preservation, preparation and metal-coating techniques allow images of the surfaces of in situ macromolecules to be obtained in a life-like state by field emission scanning – and transmission electron microscopy (FE/SEM, FE/TEM) at a resolution of 2-4 nm. A large body of macromolecular structural information has been obtained using these techniques, but while the images produced provide a qualitative impression of three-dimensionality, computational methods are required to extract quantitative 3D structure.

In order to test the feasibility of applying various photogrammetric and tomographic algorithms to micrographs of well-preserved metal-coated biological surfaces, several algorithms were attempted on a variety of FE/SEM and TEM micrographs. A stereoscopic algorithm was implemented and applied to FESEM stereo images of the nuclear pore basket, resulting in a high quality digital elevation map. A SEM rotation series of an object of complicated topology (ant) was reconstructed volumetrically by silhouette-intersection. Finally, the iterative helical real-space reconstruction technique was applied to cryo-TEM micrographs of unidirectionally heavy-metal shadowed *Gloeocercospora sorghi* filaments, resulting in a ~33 Å resolution model.

These preliminary results confirm that 3D information obtained from multiple TEM or SEM surface images could be applied to the problem of 3D macromolecular imaging in the cellular context. However, each of the various methods described here comes with peculiar topological, resolution and geometrical limitations, some of which are inherent shortcomings of the methodologies described; others might be overcome with improved algorithms. Combined with carefully designed surface experiments, some of the methods investigated here could provide novel insights and extend current surface-imaging studies. Docking of atomic resolution structures into low-resolution maps derived from surface imaging experiments is a particularly exciting prospect.

November 2006

DECLARATION

I declare that *The feasibility of high-resolution, three-dimensional reconstruction of metal-coated surfaces in structural biology* is my own work, that it has not been submitted before for any degree or examination in any other university, and that all the sources I have used or quoted have been indicated and acknowledged as complete references.

Jeremy David Woodward

November 2006

Signed: . . . . . .

ACKNOWLEDGEMENTS

I would like to thank my supervisor Professor Bryan Trevor Sewell for his enthusiasm and tireless effort toward developing the field of structural biology in South Africa.

I am grateful to Ms. Miranda Waldron for patiently demonstrating the use of the scanning electron microscope, preparing samples and always being at hand to answer questions. Many thanks also to Dr. Frederick Nicolls for explaining to me the principles of photogrammetry and my fellow students for helpful discussions and support.

I would like to thank my family for their continued support and encouragement.

Finally, I gratefully acknowledge the financial assistance of the Carnegie Corporation of New York and the National Research Foundation.

LIST OF ABREVIATIONS

TEM	Transmission electron microscope
FETEM	Field emission transmission electron microscopy
SEM	Scanning electron microscope
FESEM	Field emission scanning electron microscopy
EM	Electron microscopy
FSC	Fourier shell correlation
IHRSR	Iterative helical real-space reconstruction
SNR	Signal-to-noise ratio
DEM	Digital elevation map
2½ D	2½ dimensional, matrix of elevations representing a 3D object
3D	Three-dimensional
SIRT	Simultaneous Iterative reconstruction technique
NPC	Nuclear pore complex
NPB	Nuclear pore basket
ATP	Adenine triphosphate
VRML	Virtual reality modelling language
NMR	Nuclear magnetic resonance
CHT	Cyanide hydratase
HCN	Hydrogen cyanide
BSE	Back-scattered electrons
SE	Secondary electrons
CAM	Cell-adhesion molecule

TABLE OF CONTENTS

CHAPTER 1

GENERAL INTRODUCTION

1.1 Low resolution data in structural biology

One of the long-term goals of structural cell biology is the integration of atomic and cellular resolution information in order to identify and interpret the molecular interactions that underlie cellular processes (e.g. Baumeister 2005). Techniques with the capacity to image cells in lifelike conditions, three-dimensionally at resolutions sufficient to distinguish the structural signatures of particular macromolecular-complexes from those of other, possibly similar, structures (Medalia *et al*., 2002) have the potential to contribute to our understanding of cellular function by "bridging the resolution gap". By docking higher-resolution structures of large macromolecular complexes, generated by x-ray crystallography, nuclear magnetic resonance (NMR) spectroscopy, single-particle electron tomography, modelling or combinations of these techniques, into lower-resolution cellular data, pseudo-atomic resolution data can be generated of macromolecular complexes, organelles or even whole cells (Bohm *et al*., 2000).

The constituent components of macromolecular complexes often function interchangeably and remodel in response to specific signals or changes in the physiological state of the living cell. Supra-atomic resolution data can help to validate interaction models between proteins, and facilitate the elucidation of conformational changes occurring in protein complexes (e.g. Aloy *et al*., 2004). In order to study these changes, the living cell is perturbed by varying environmental parameters or substrate concentrations, and then rapidly vitrified to capture a "snapshot" of the dynamic cellular events taking place at time intervals of several milliseconds. Low-

resolution data is generated and high-resolution (atomic resolution, if available) components are docked into the resulting 3D maps. The result is a pseudo-atomic resolution structure, perturbed in a controlled way (e.g. Saibil, 2000).

For one class of proteins: those which are not amenable to either x-ray crystallography of bio-molecular NMR, lower resolution techniques may be the only available method for obtaining structural information (Baumeister and Steven, 2000). This problem is fundamentally different from those posed above: where atomic resolution information is available and it is the locality or conformation of a known macromolecule that is under investigation. Information about the dimensions, stochiometry and arrangement of subunits or even the morphology of individual subunits within a macromolecule can be investigated depending on the resolution of the structural information available and size of the macromolecular complex under investigation (Frank, 2006). This low-resolution molecular information can provide valuable insights into the functioning of macromolecular complexes.

1.2 The scanning electron microscope

The modern field emission scanning electron microscope (FESEM) is capable of imaging the surfaces of cryo-immobilized, metal-coated biological specimens with a resolution down to 20-40 Å (2-4 nm) as a function of physiological structure (reviewed by Hermann and Muller, 1997). Rapidly vitrifying samples by cryo-plunging or high-pressure techniques captures surface molecules in the hydrated state (e.g. Erlandsen *et al*., 2001) and a variety of fixation and stabilization methods, combined with appropriate cryo-metal coating techniques, allow direct visualization of surface macromolecules (e.g. Jeffree *et al.*, 2003). FE/SEM micrographs can be

acquired at a wide magnification range allowing samples to be viewed from the tissue – to the macromolecular level. This allows areas of interest to be identified at low magnification for high magnification study (Pawley, 1997).

A fine electron beam is produced, accelerated and focussed by the electron gun and a series of electron lenses in the column of the FE/SEM. Deflection coils scan the beam in a raster across the surface of the specimen while, perpendicularly, the position of the scan is advanced incrementally (Pawley, 1997). While a variety of signals are produced when the electron beam impinges on the sample, the secondary electron (SE) – and backscattered electron (BSE) signals are of greatest importance when investigating the topology of a sample (Cazaux, 2005). The intensity of the relevant signal (SE or BSE) and position of the electron beam on the specimen as a function of time corresponds to a given pixel intensity in the resulting image. The resolution limit of the imaging system depends on the electron beam diameter at the sample as well as the depth from which detected electrons originate, while maintaining adequate beam current (Pawley, 1997). Within these conflicting constraints, the strategy undertaken depends on whether SE or BSE are detected.

1.2.1 Backscattered electron imaging

BSE are elastically scattered and range in energy from 50 kV to the beam energy, the intensity of the BSE signal is a function of atomic number (Z) (termed Z-contrast) and to a lesser extent, specimen tilt (Cazaux, 2005). Topographic information is obtained by shadowing the sample unidirectionally with metal. The thickness of the metal coating, and consequently the intensity of the image at a given location, is dependent on the surface normal of the sample at that location (Cazaux, 2005). High-resolution

micrographs have been obtained of thin cryo-samples at high accelerating voltage using this method. The results are analogous to those of the TEM-replica technique (Walther and Muller, 1997). Bulk samples have also been imaged at high resolution using the BSE_I signal by lowering accelerating voltages; this is possible with the FESEM operated at high emission current (Richards *et al.*, 1999).

1.2.2 Secondary electron imaging

SE's are inelastically scattered sample electrons that arise near to the surface of the specimen, with energies below 50kV (Pawley, 1997). By lowering the accelerating voltage, the electron beam penetration depth is lowered, which biases the signal towards SE_I (Stokroos *et al*., 1998). An ultra-thin (<1nm) metal film applied onto the sample helps to localize the surface signal (SE_I), stabilise features and decrease specimen charging (Stokroos *et al*., 1998). In contrast to BSE images, the SE coefficient is relatively insensitive to atomic number. SE image contrast is chiefly a function of the surface normal at each position on the sample, modulated by the probability of electron escape (Pawley, 1997). To a first approximation, topographic information in the form of surface normals can be derived (Beil and Carlson, 1991), being a function of micrograph intensity. However, at high magnification (>100 000×) the beam interaction volume may approach specimen feature volume resulting in delocalization of the SE signal and anomalous contrast effects (Pawley, 1997).

1.3 The transmission electron microscope

Freeze-drying and unidirectional heavy metal shadowing is an established procedure for investigating biological macro-molecular surface structure (Gross *et al*., 1990). FE/TEM micrographs of samples prepared using these methods display excellent

signal to noise ratio, allowing direct observation of structures at resolutions down to ~20 Å (2 nm) (Hoenger *et al*., 2000). Optimal preservation is achieved with thin, beam-transparent specimens, which can be observed directly in the frozen state after metal shadowing (Gross *et al*., 1990). While metal casts derived from thick samples require a cleaning step prior to viewing (e.g. Walther and Muller, 1997). However, the result is equivalent, in terms of the topological information that can be extracted; in the form of surface normals. This information, combined with image processing methods, is commonly used to derive three-dimensional surfaces in the form of digital elevation maps (DEMs) by surface relief reconstruction (Guckenberger, 1985).

1.4 Surface macromolecular structure

1.4.1 Macromolecular structure visualised by scanning electron microscopy

Despite a paucity of published FESEM macromolecular resolution studies, two outstanding examples exist: The nuclear pore complex and cell adhesion molecules. Interestingly, these two studies apply completely different methodology and fulfil different low-resolution structural aims.

1.4.1.1 The nuclear pore complex

Ris (1989) imaged the surface of dehydrated, critical point dried, platinum coated nuclear envelopes from frog and newt oocytes using the SE signal at low voltage in the FESEM. The resulting micrographs clearly demonstrate the overall arrangement of the outer surfaces of the nuclear pore complex (NPC) with extraordinary clarity (reviewed by Lim *et al*., 2006). This preparative procedure allows imaging at high resolution under high-dose conditions providing rich low-noise images. Allowing individual micrographs to be examined without averaging, facilitating structural

description of flexible components (figure 1.4.1.1 A, B). The limitation of this method is that only the outer surface of the NPC is accessible to imaging; a limitation overcome by uncovering the underlying structure by proteolysis, detergent extraction and mechanical disruption (Goldberg and Allen, 1993; 1996). This allows visualisation of underlying structure by a process of "molecular dissection".

More recently the functional dynamics of the NPC has been explored by varying conditions and substrates before imaging. These perturbation experiments provide valuable information about the functioning of the complex. Goldberg *et al*. (1999) visualised NPC conformation changes resulting from the addition of Ran. The resulting structural changes at the level of individual filaments could be visualised at high resolution by FESEM. The potential of surface imaging of the NPC by low-voltage FESEM lies in the high resolution and low-noise imaging of individual particles, without averaging or symmetry imposition.

1.4.1.2 Cell-adhesion molecules

Erlandsen *et al* (2001) used BSE imaging with high-resolution cryo-field emission SEM (cryoFESEM) to differentiate between three different cell-adhesion molecules (CAMs) on the surface of human leukocytes (figure 1.4.1.1 C). After rapid vitrification and partial freeze-drying, the spread leukocytes were shadowed with 2 nm of tantalum/ tungsten at 45º followed by a ~7-10nm layer of carbon. The P-selectin (CD62P); GPI-IX complex (CD42a,/CD42bα,bβ) and GPIIb-IIIa (CD41/CD61) could be identified by heights determined by stereo parallax differences using Stereocon® software (Marko and Leith, 1996) (figure 1.4.1.1 C).

Colloidal gold labels provided positively identifiable locations whereby the detection accuracy rate of the stereo method could be estimated (figure 1.4.1.1 D).

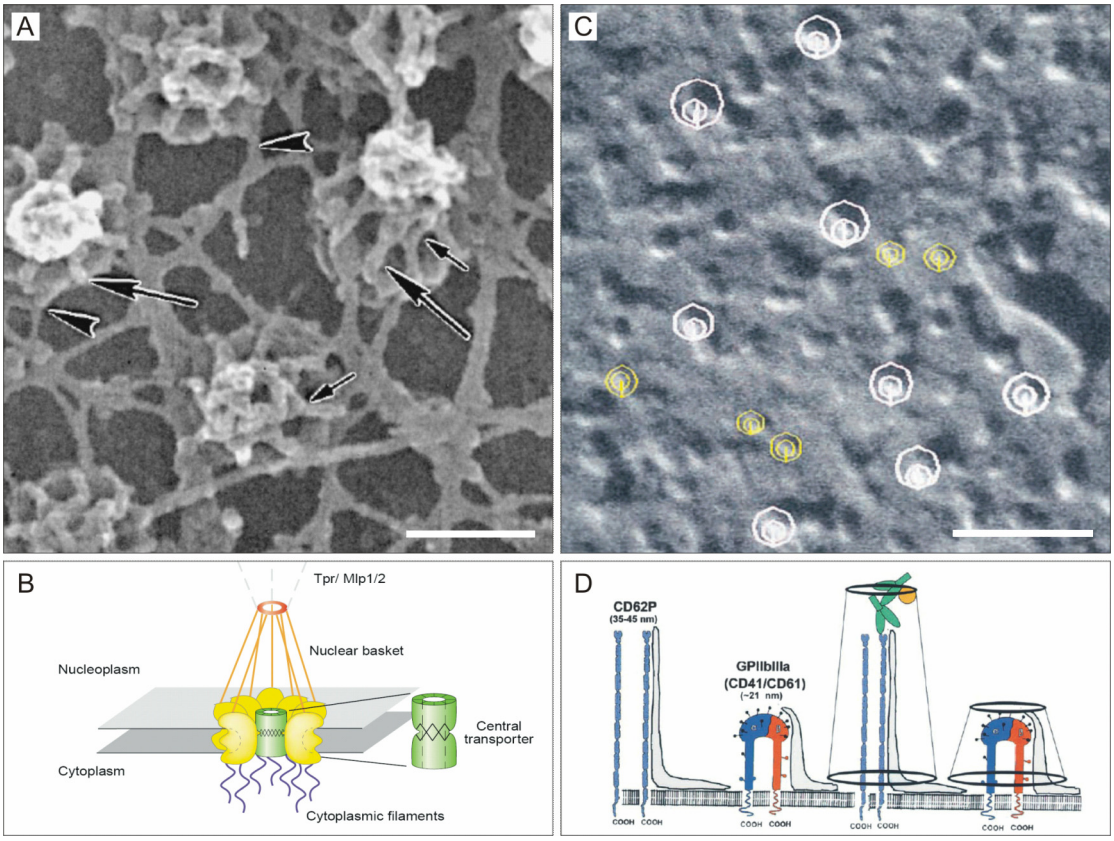

Figure 1.4.1.1 (**A**) SE low-voltage FESEM image of the nucleoplasmic side of the nuclear envelope, individual NPB can be seen; arrows indicate various features of the basket filaments (from Goldberg and Allen, 1996). (**B**) Model of the nuclear pore complex, the nuclear basket is shown in orange (from Vasu and Forbes, 2001). (**C**) The high-resolution surface of a vitrified and unidirectionally shadowed human leukocyte viewed with the BSE signal of the FESEM. Individual cell adhesion molecules (CAMS) are identified by their projection above the membrane. (circles) (from Erlandsen *et al*., 2001). (**D**) Schematic illustration of the shadowing process, CAMs can be distinguished from one another based on their stereoscopically estimated projection above the membrane (from Erlandsen *et al*., 2001). Scale bars: 100 nm.

1.4.2 Macromolecular structure visualised by transmission electron microscopy

Macromolecular imaging by metal-shadowing TEM is a well-established technique for exploring the surfaces of *in situ* cell structure as well as that of purified macromolecules (Fuchs *et al*., 1994). A few examples have therefore been chosen to illustrate the type of experiments being performed and the quality of the resulting data.

1.4.2.1 Freeze-fractured whole cells

Only structures exposed to the surface are available for imaging; internal structures such as membrane – or cytoplasmic proteins must be exposed by freeze-fracture and/ or deep-etch methods (Southworth *et al*., 1997). Fractured membranes from rapidly vitrified individual cells are shadowed with metal; the resulting replicas are cleaned before viewing by TEM. The resulting images show the distribution of trans-membrane – and cytoplasmic proteins. Similar methods have been successfully applied to tissue samples such as myocardial tissue (Frank *et al.*, 1987). A large number of studies exist and the methods applied have become routine (Frank *et al*., 1987), vast quantities of data are generated and unfortunately only analysed descriptively. With no method available to identify individual macromolecules in the membrane, these types of experiments will remain of limited use.

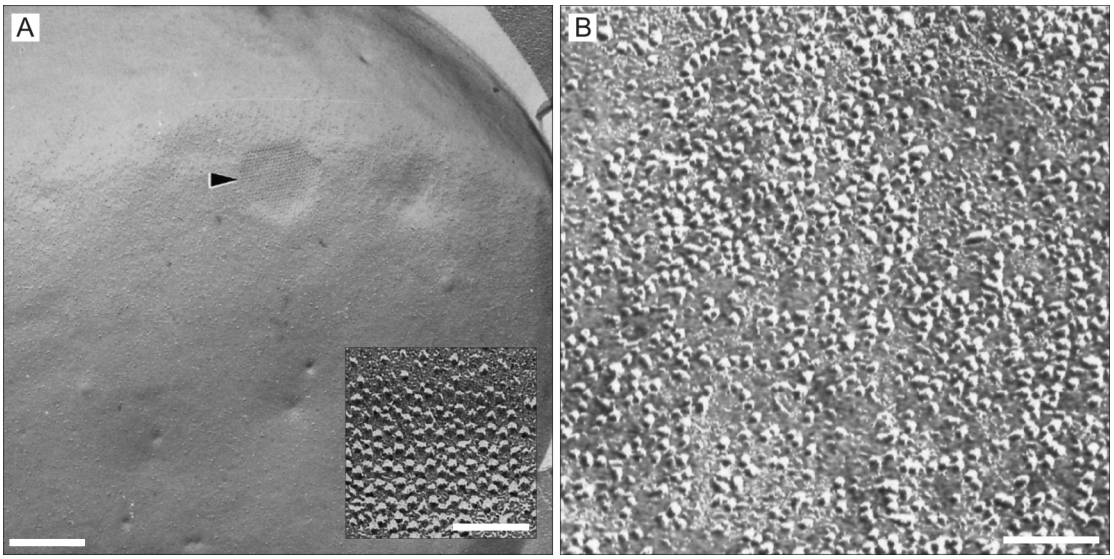

Figure 1.4.2.1 (**A**) Freeze-fractured, unidirectionally shadowed sperm membrane from *Plumbago zeylanica.* An ordered region marked with an arrow is shown at higher magnification in the inset. (from Southworth *et al*., 1997). (B) Vitrified, freeze-fractured unidirectionally shadowed myocardial sarcolema. Individual trans-membrane proteins are visible protruding from the fractured membrane surface (from Frank *et al*., 1987). Scale bars: 500 nm (A), 100 nm (inset), 100 nm (B).

1.4.2.2 Two-dimensional crystalline surface imaging

The advantage of imaging crystals is that averaging is readily achieved in Fourier (Crowther and Klug, 1975) – or real space (Smith and Kistler, 1977) and therefore electron dose can be kept low (Fuchs *et al*., 1994). Applying crystallographic symmetry operators is equivalent to shadowing from multiple directions and therefore all of the information required to calculate a relief map can be acquired from a single image (e.g. Rockel *et al*., 2000; Walz *et al*., 1996; Gross *et al*., 1990; Fuchs *et al*., 1994). The handedness ambiguity associated with negative-stain – or cryo-projection methods can be resolved with shadowed-data (Walz *et al*., 1996).

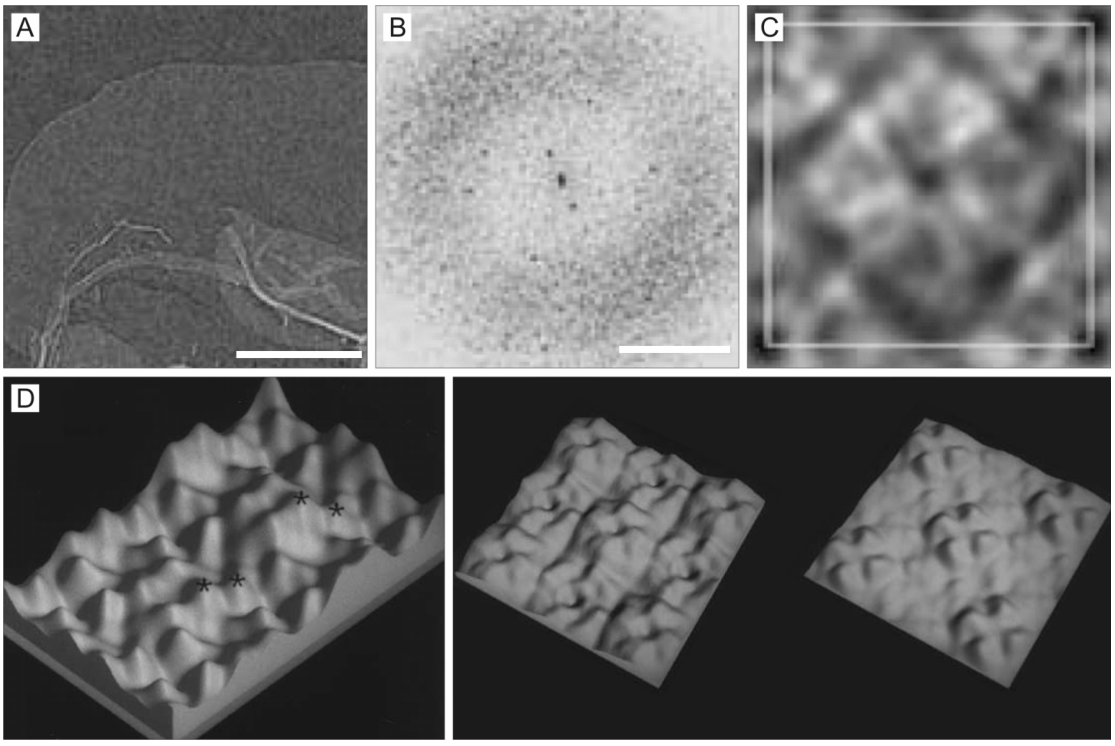

Figure 1.4.2.2 (A) Low dose unidirectionally shadowed micrograph of the surface of a two-dimensional membrane-bound aquaporin-1 crystal. (B) The power spectrum derived from A. (C) Correlation averaging of A results in an improvement in SNR. The unit cell, indicated by a square has a side length of 9.6 nm. (D) Examples of digital elevation maps (DEMs) derived from C. The handedness of individual aquaporin-1 molecules could be determined (from Walz *et al*., 1996). Scale bars represent: 0.5 μm (A), 2.5 nm^{-1} (B); length of sides: 19.2 nm (C), 9.6 nm and 20.6 nm (D).

1.4.2.3 Isolated macromolecules

Purified symmetrical macromolecules that preferentially adhere to the substrate in a particular orientation have been studied and reconstructed by unidirectional metal shadowing (Rockel *et al*., 2000). The method includes classifying particles into classes consisting of different shadowing directions, allowing surface relief reconstruction to be performed (figure 1.4.2.3 A, B, C). Recently, improved reconstructions have been acquired by applying the random conical tilt method to preferentially oriented single particles (Lanzavecchia *et al*., 1998). This method results in a full 3D reconstruction of the metal cast resulting from shadowing. The protein core is computationally extracted from the cast by thresholding, resulting in a high quality model (figure 1.4.2.3 D, E, F).

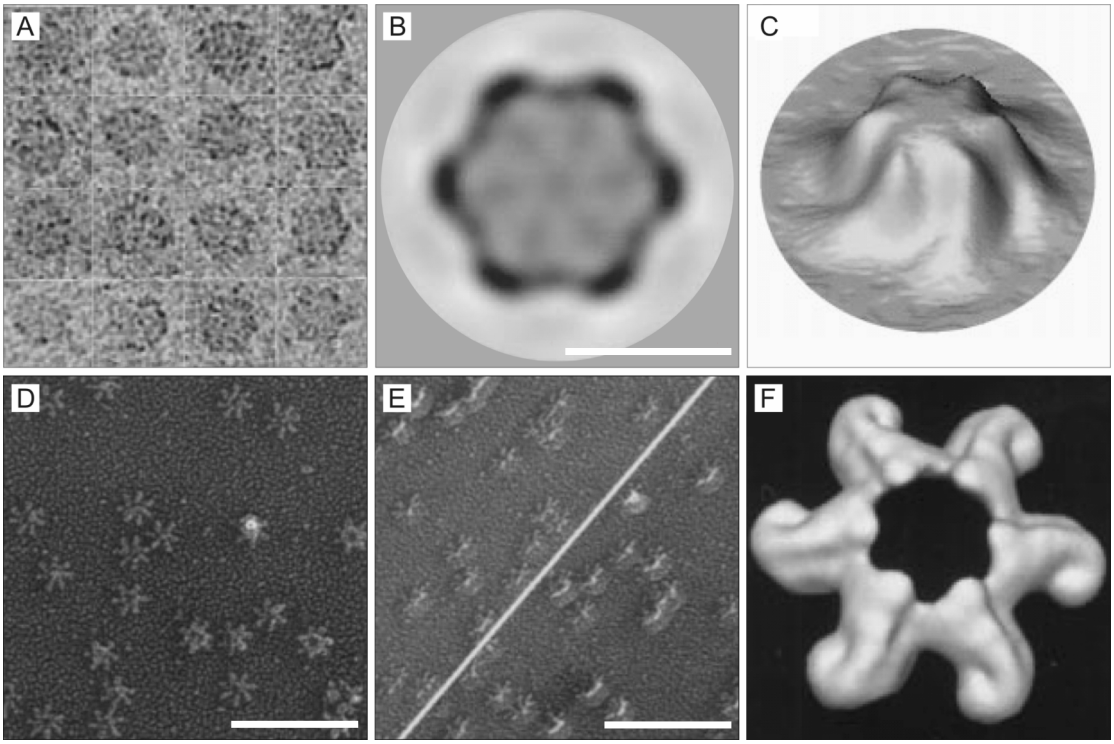

Figure 1.4.2.3 (**A**) Low dose micrographs of unidirectionally metal shadowed VAT particles. (**B**) Averaged, six-fold symmetrised particles. (**C**) 1.5 nm resolution digital elevation map calculated from classified images. (from Rockel *et al*., 2000). (**D**, **E**) Untilted and tilted micrographs of rotationally shadowed *heliobacter pylori* vacuolating cytotoxin. (**F**) Reconstructed metal-cast resulting from random-conical tilt tomography (from Lanzavecchia *et al*., 1998). Scale bars: 10 nm (B/C), 100 nm (D,E/F).

1.4.2.4 Reconstituted cellular components

Imaging of reconstituted cellular components is a rather fruitful methodology for studying the interactions between different proteins and cellular components. Matsuoka *et al*., (2001) studied COPII coated vesicles by deep-etch cryo-metal shadowing. Purified protein, microsomes and GMP-PNP were used to generate vesicles *in vitro* and the assembly of COPII vesicles were compared to clathrin-assembly (figure 1.4.2.4 A). Mullins *et al*., (1998) viewed Arp2/3 bound to actin at junctions. Samples were absorbed onto mica, rapidly vitrified and freeze-dried before unidirectional shadowing. The resulting images show actin junctions at sufficient resolution to identify individual components (figure 1.4.2.4 B). Volkmann *et al*. (2001) extended this study by manually fitting an atomic resolution structures as well as a single particle reconstruction of the Arp2/3 complex into an average of the Arp2/3-actin complex visualised by cryo-metal shadowing.

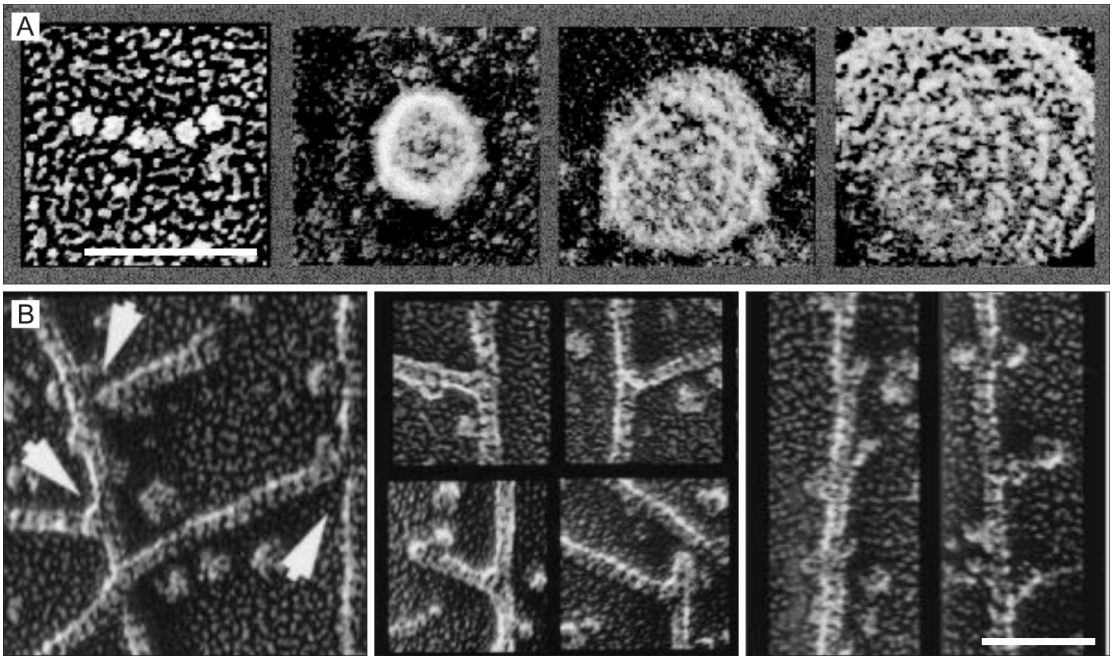

Figure 1.4.2.4 (A) A series of low-angle rotationally shadowed micrographs of COPII and membrane, COPII interacts with the membrane to form a vesicle (from Matsuoka *et al*., 2001). (B) Quick-frozen and deep-etched rotationally shadowed actin filaments in complex with Arp2/3 (from Mullins *et al*., 1998). Scale bar: 50 nm (A), 40 nm (B).

1.5 Conclusion and aims

While micrographs provide some indirect 3D information and may have the appearance of three-dimensionality, computational methods are required to extract quantitative 3D information (e.g. Piazzesi, 1973; Guckenberger, 1985; Crowther and Klug, 1975). 3D data has been extracted from various FE/SEM and FE/TEM metal-coated micrographs using surface-normal information from SEM micrographs: "shape from shading" (Beil and Carlson, 1991) and metal-shadowed TEM micrographs: "surface relief reconstruction" (Guckenberger, 1985). Stereoscopy has been applied to SEM micrographs (Piazzesi, 1973; Stampfl *et al.*, 1996) and tomography has been applied to TEM replicas (Lanzavecchia *et al*., 1998). These methods have been inconsistently applied; for instance, no stereoscopic method has been applied to macromolecular FESEM micrographs. Other methods that have been developed for the reconstruction of geometric models from photographs, such as volumetric reconstruction methods have not been applied at all to microscopic data.

The problem of reconstructing FESEM biological macromolecular data is considered for the first time and a stereoscopic algorithm is implemented and optimised for FESEM micrographs and applied to previously published FESEM micrographs of biological macromolecules. A novel method, which includes identifying and extracting areas of low electron escape probability, is developed and used to improve the resulting reconstructions.

Surface normal data are extracted from SEM data and compared to the theoretical surface normals for objects of the same geometry. The various options available for refining stereoscopic SEM data by using surface normals are considered.

A novel backprojection method that uses the simultaneous iterative reconstruction technique (SIRT) is applied to silhouetted SEM micrographs of an object of complicated topology (an ant). The problem of imperfect silhouetting of noisy micrographs is considered and a method is developed whereby a probability is assigned to each pixel before optimisation by the SIRT algorithm.

The iterative helical real-space reconstruction (IHRSR) technique was applied to TEM images of freeze-dried unidirectionally shadowed helices.

CHAPTER 2

FE/ SEM STEREO RECONSTRUCTION

2.1 Introduction

The nuclear pore complex (NPC) is a large (~120 million Daltons in vertebrates) macromolecular assembly that mediates the signal-dependant bidirectional transport of macromolecules across the nuclear membrane (reviewed by Wente, 2000). NPCs allow passive diffusion of ions and small molecules with diameters < 9 nm (Peters, 1986) and selectively transport macromolecules between 9 – and 39 nm in diameter in a signal-mediated manner (Pante and Kann, 2002). Import into the nucleus is initiated by the binding of a protein containing a nuclear localization signal (Richardson *et al*., 1988) to a receptor on the cytoplasmic side of the NPC. Active transport across the NPC is ATP-dependant (Garcia-Bustos *et al*., 1991) and occurs through an unknown mechanism (e.g. Vasu and Forbes, 2001). It is hypothesized that translocation occurs through a process of sequential binding of different nucleoporins.

The structure of the NPC has been extensively studied by FESEM using the methodology developed by Ris (1989). This involves the extraction of frog or newt oocytes, which are fixed, dehydrated in ethanol, critical point dried and sputtered with a thin layer of metal before viewing, at low voltage, in the FESEM. This technique demonstrated, for the first time, the asymmetry that exists between the cytoplasmic and nucleoplasmic sides of the nuclear pore complex (reviewed by Lim *et al*., 2006). The nucleoplasmic side displays a basket or fishtrap structure (Ris, 1989), the nuclear pore basket (NPB) which is comprised of eight ~75 nm filaments supporting a ~50 nm ring. Although cryo-tomographic reconstructions of the NPC exist (Stoffler *et al*., 2003; Beck *et al*., 2004; Yang *et al*., 1998), the basket filaments are disordered,

because of the large structural variability of these structures and therefore a 3D map of the NPB is not available.

Lim *et al*. (2006) have suggested that a complete structural characterization of the NPC will be achieved as the result of a combination of multiple methodologies, each yielding incomplete but complementary structural information. To this end we have suggested extracting 3D surface data from previously published stereo micrographs of the nuclear pore basket. An algorithm for converting pairs of images into digital elevation maps, based on the method described by Stampfl *et al.* (1996) was developed, tested and optimised for FESEM of biological samples. SEM micrograph stereo pairs of an Argentinean ant *Linepithema humile*, were used to test the initial algorithm and optimise the parameters, the working algorithm was then applied to stereo images of the nuclear pore basket from Goldberg and Allen (1993; 1996).

2.1.1 Aims

1) Develop and test a stereo reconstruction algorithm and optimise it for FESEM data.
2) Use published FESEM stereo pairs of the nuclear pore basket from *Xenopus* oocytes to generate a 2½ dimensional digital elevation model (DEM) of this structure.

2.2 Research design and methodology

2.2.1 Photogrammetry

Piazzesi (1973) introduced the formulation for the acquisition of three-dimensional information from stereo scanning electron images. At constant inter-micrograph magnification, a minimum of two micrographs with six relative orientation parameters: x, y and z translations and three Euler angles are required. At high

magnifications (>1000×), orthographic projection is approximated, which negates the need for a z translation and reduces the necessary parameters to five. In practice, the sample is usually tilted about a single axis without translation, further simplifying the necessary requirements to a single parameter. The 3D coordinates of each pixel are calculated by triangulation between homologous points on each micrograph (Piazzesi, 1973) (figure 2.2.1.1). The result, a matrix with the x and y dimensions of the original images comprising z heights, is referred to as a 2½ dimensional *digital elevation map* (DEM) (Lucas and Kanade, 1981).

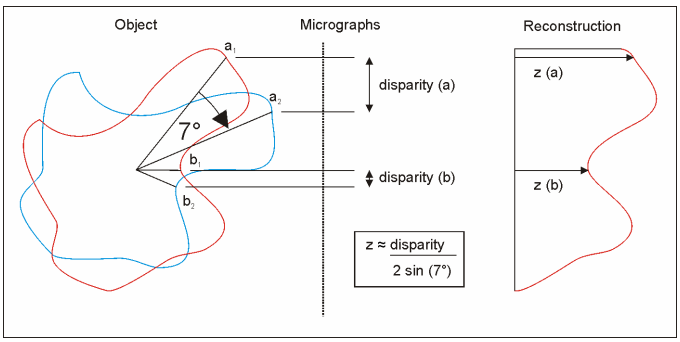

Figure 2.2.1.1 The method of Piazzesi (1973). Homologous points are identified on two images (red and blue) before and after rotation of the sample (*reference* and *matching* images respectively). The difference in horizontal position of homologous pixels is used to calculate disparity values, which are converted into z heights. The x and y positions are taken from the reference image and the angle of rotation is obtained from the stage micrometer of the FE/ SEM.

The identification of homologous pixels on stereo images is referred to as the *stereo correspondence* problem or the *stereo registration* problem and the solution procedure is generally called *matching* (e.g. Belhumeur and Mumford, 1992). Ideally, matching results in the identification of a corresponding pixel in the matching image for every pixel in the reference image (figure 2.2.1.2).

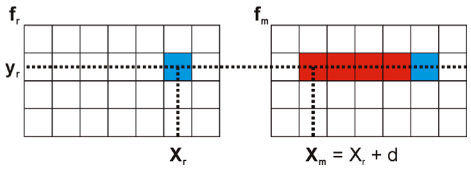

Figure 2.2.1.2 A pixel (x_r,y_r) in the reference image (f_r) is matched to the homologous pixel (x_m,y_r) in the matching image (f_m). The disparity (d) is given by $d = x_m - x_r$ (from Gallo and Binaghi, 2005).

Figure 2.2.1.2 illustrates the stereo correspondence problem for a special case where the image *epipolar lines* lie along the horizontal axis, simplifying the matching procedure to a one-dimensional search along the x-axis (e.g. Kammerud *et al*, 2005). This geometry approximates that obtained when a sample is tilted about a single axis, perpendicular to both the beam axis and the image axis, at high magnification in the FE/ SEM. The epipolar lines will, in this case, lie approximately along one of the axes of the resulting stereo-micrograph pair. This procedure is implemented in SEM stereo algorithms by Piazzesi (1973); Stampfl *et al*. (1996, 2002); Bethel & Bastacky (1999); Scherer & Kolednik (2001) and generally results in good quality DEMs.

The FE/ SEM offers obvious advantages when performing photogrammetry: sub-pixel geometric distortion, wide magnification range, large depth of field and parallel projection (at high magnification) (Hemmleb and Schubert, 1997). Nevertheless, under the conditions necessary for macromolecular structural determination certain artefacts become apparent: blurring obscures detail near the resolution limit of the microscope and the signal: noise ratio (SNR) may be poor, a consequence of imaging at low dose. Charging and edge effects may drastically change the appearance of homologous points between micrographs leading to mismatches. The problem of half-occluded points that do not have corresponding positions in both images (Belhumeur & Mumford, 1992) must be dealt with. Furthermore, sample regions with low electron

escape probability, containing little or no topographic information lead to large mismatched areas.

2.2.2 Developing and testing the algorithm

When surfaces are approximately continuous, with good texture, area-based matching methods can be successfully applied (Lucas and Kanade, 1981). The ideas of Frankot *et al*. (1994) formed the basis of the algorithm. The method consists of deriving a search window from one of the images (reference image), which is cross-correlated with the other image (matching image). The coordinate with the highest correlation coefficient is assumed to represent the homologous point (Frankot *et al*., 1994). The algorithm was implemented in Matlab V6.5 ©Mathworks Ltd.

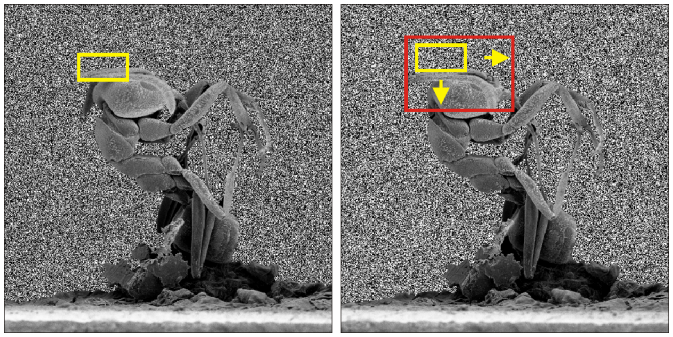

Figure 2.2.3 Stereo algorithm, the search window (yellow) was cross-correlated with an area on the matching image (red). The x-dimension of the search area on the matching image corresponds to the expected disparity and the y-dimension corresponds to the expected deviation from horizontal epipolar lines. A 470×470 pixel image pair took ~2 hours of processing time (3.2 GHz CPU 1 Gb Ram) to match.

For each pixel matched, the y-deviation between the reference and matching image is recorded; this indicates problems in the initial alignment of the reference and matching images and the extent of the deviation from the assumption that the image epipolar lines lie along the x-axis. It was noted early on, that deviations from epipolar geometry and alignment errors could be ignored.

The number of grossly mismatched pixels, visible as outlying peaks in the DEM was minimised by optimising four parameters:

1) The size of the search window
2) The correlation coefficient threshold below which a given pixel is assumed to be incorrectly matched
3) The maximum z dimension range (disparity) of the sample
4) The size of the median filter applied to remove incorrect matches

1) The size of the search window is a critical parameter; a larger search window is more likely to identify the correct matching point, having a larger sample size from which to identify the correct solution. But the overall resolution will be worse, the point being an average of a larger area. A ratio of 1.5: 1 (x: y) was chosen for the search window, the x dimension being larger because image rotation occurs about the y-axis and therefore a greater difference between reference – and matching-images is found in the x-dimension. A sample of pixels were manually matched and compared to the results obtained by automated matching. The smallest window required to correctly identify the manually matched pixels was identified (15 × 11 pixels).

2) The correlation coefficient threshold needs to fulfil two conflicting demands: to minimize mismatched pixels (type II statistical error) while reducing correct matches that are eliminated (type I statistical error). A correlation threshold of 0.4 was chosen: with a sample size of 165 (search window dimensions: 15 × 11 pixels), this corresponds to a probability of $p = 0.001$ that the correlation occurred by chance. However, with a sample size of 470 × 470 pixels, SEM imaging artefacts and half occluded points, a large number of false matches still arise.

3) The maximum z-dimension of a sample helps to identify mismatched points and define an expected disparity to limit the search range. This approach decreases computational time as well as improving matching accuracy.

4) The remaining outliers are removed by applying a median filter. The size of the filter must be optimised, too large and critical detail is lost, too small and a large number of outliers escape detection. The DEM is then low-pass Fourier filtered to remove remaining high frequency noise (outliers) and sharp edges. The method of Piazzesi (1973) is used to calculate the three-dimensional coordinates from the resulting disparity map.

2.2.3 Stereo reconstruction of an Argentine ant, Linepithema humile

The algorithm was tested on a stereo micrograph pair of an Argentine ant, *Linepithema humile* (see section 3.2 for details). The normalised cross-correlation between the 15 × 11 pixel search window derived from the reference image with the matching image produces a large peak that can be distinguished from spuriously correlating pixels (figure 2.2.3.1 A, B). Below the threshold value of 0.4, a large number of spurious correlations are present (figure 2.2.3.1 B). This type of plot can indicate whether or not the search window is sufficiently large and whether or not the correlation threshold is appropriate.

The value of the normalised cross-correlation peak at each point in the reference image is indicated in figure 2.2.3.1 C, D. Figure 2.2.3.1 C displays spuriously high correlation coefficients along the edge formed by the dark background (figure 2.2.3.1

E) In fact the correlation coefficients along the periphery of the object should be lower than that obtained by internal details. This is because the object is rotated between the reference – and matching-images and therefore the edges cannot be matched correctly, as they are not common between the two images. This situation is improved by adding noise to the background (figure 2.2.3.1 D, F).

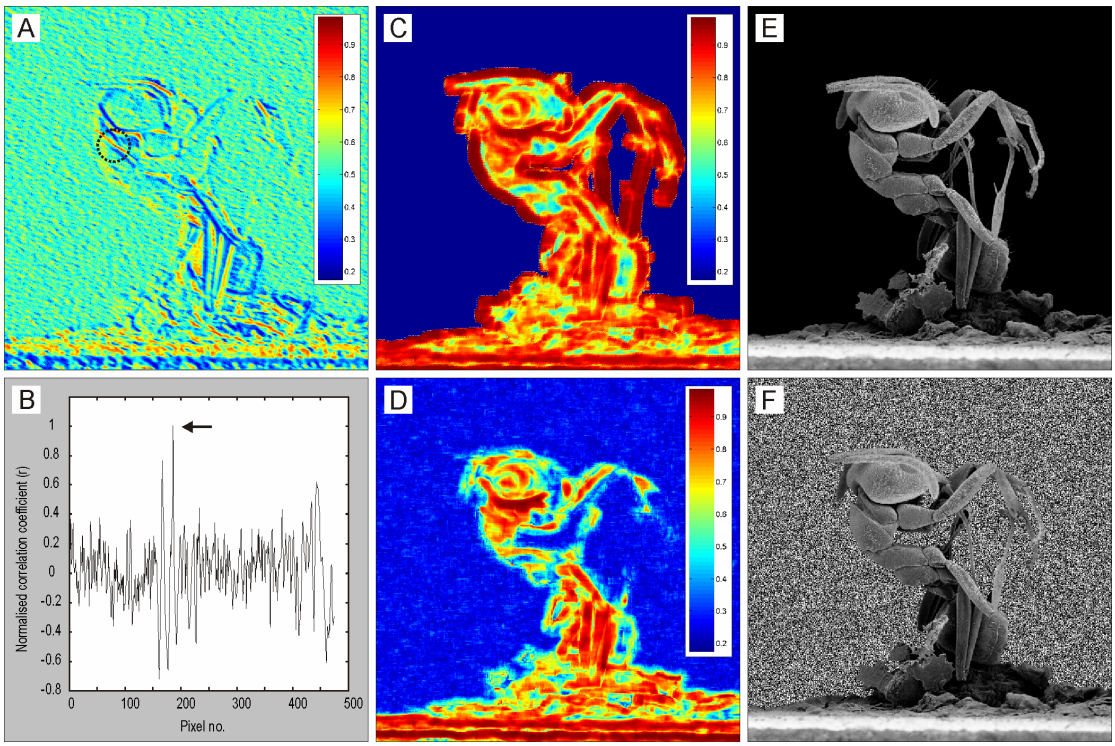

Figure 2.2.3.1 (**A**) Normalised cross-correlation function calculated between a 15×11 pixel search-window derived from the reference (left) image and the matching (right) image (see fig. 2.2.3.2 A). The global maximum, indicated by a circle, corresponds to the pixel assumed to be the homologous point on the matching image. (**B**) Plot of a vector taken along the y-axis of the matrix in (A): an arrow indicates the peak position. (**C, D**) Matrices of cross-correlation peaks; the position of each peak corresponds to the reference image shown in (E) and (F) respectively. The matrix values correspond to the normalised cross-correlation peak associated with that point. Anomalously high correlations are present along the edge of the silhouette in (C). These originate from the large differences visible in (E) between background – and foreground pixel intensity. (D) By adding Gaussian noise to the background see (F), these anomalously high correlations have been successfully eliminated. (**E**, **F**) Reference images with and without noise.

The micrograph stereo pair with noise added to the background (figure 2.2.3.2 A) generated the disparity map shown in figure 2.2.3.2 B. This was 3 × 3 median – (figure 2.3.2 C) and Guassian-filtered to remove sharp edges and high frequency noise, the formulation of Piazzesi, 1973 was used to calculate a DEM (figure 2.2.3.2 D). The 2½ D geometry of the digital elevation map is not appropriate for describing

the complex geometry of the ant. However, 3D surface coordinates can be extracted, within the limitations of the methods, and used to calculate linear distances.

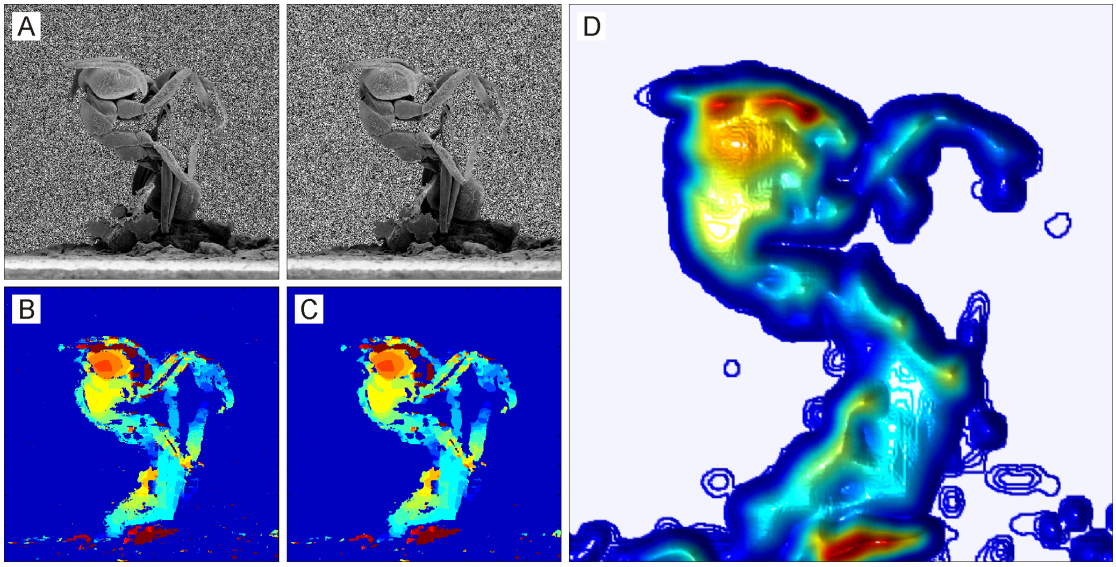

Figure 2.2.3.2 (**A**) Stereo pair of images, separated by a rotation of approximately 7º, the background of both the images has had noise added to prevent spurious correlations (see figure 2.2.3.1 C, D, E, F). (**B**). Disparity map derived from differences in the x-coordinates of homologous points in the stereo pair. (**C**) The disparity map after application of a 3×3 median filter to reduce noise. (D) The median-filtered disparity map was low-pass Fourier-filtered and used to calculate x, y and z coordinates on the surface of the subject by the method of Piazzesi (1973) yielding a low resolution 2 ½ dimensional reconstruction.

2.2.4 Surface normal extraction

An aluminium plate was tilted while images were captured at ~ 5º intervals to measure the relationship between the angle of a sample relative to the beam, and the recorded intensity in the SEM; the result is shown in figure 2.2.4.1. In order to test how applicable this normal information is to the refinement of high-magnification samples, a spherical latex bead was imaged at high magnification in the SEM and compared to theoretical normal values calculated on the surface of a perfect sphere. The results are shown in figure 2.2.4.2.

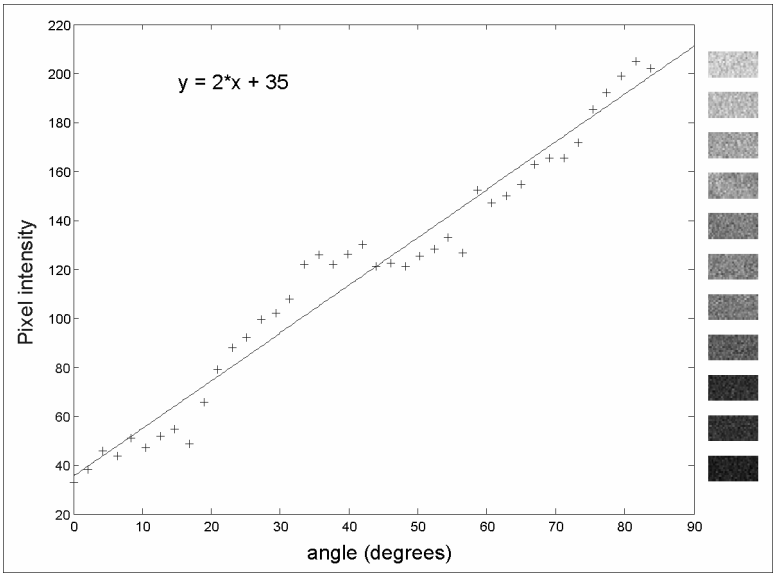

Figure 2.2.4.1 The relationship between pixel intensity (shown on the right) and the angle of the stage of the LEO S440 SEM. This information can be used to extract ambiguous surface normal information from SEM images; multiple images of the same object from different angles resolve this ambiguity, allowing the calculation of a DEM (Beil and Carlson, 1991).

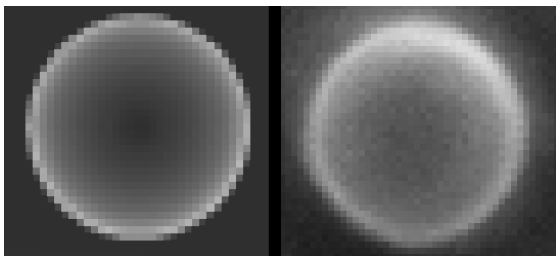

Figure 2.2.4.2 The normals on the surface of a perfect sphere, coloured according to the relationship calculated by tilting (left) compared to a latex bead imaged at high magnification in the LEO S440 SEM. The latex bead shows blurring and noise compared to the theoretical sphere.

Blurring and noise obscure some of the normal information (figure 2.2.4.2); multiple images would therefore be required. The change in intensity after rotation of points on the objects surface could be used to determine the surface normals at each point. A surface relief reconstruction strategy could then be adopted.

2.3 Results: presentation and discussion

The optimised algorithm, developed for the ant reconstruction was applied to stereo micrographs of the nuclear pore basket. The first stereo pair comes from Goldberg and Allen (1993). Several ~ 100 nm diameter nuclear pore baskets (NPB) are clearly

visible in the raw images (labelled in the matching image) (figure 2.3.1 A). The nuclear membrane, is not present as the sample has been extracted with detergent and cannot be successfully matched, as is the case between individual basket filaments (see figure 2.3.4).

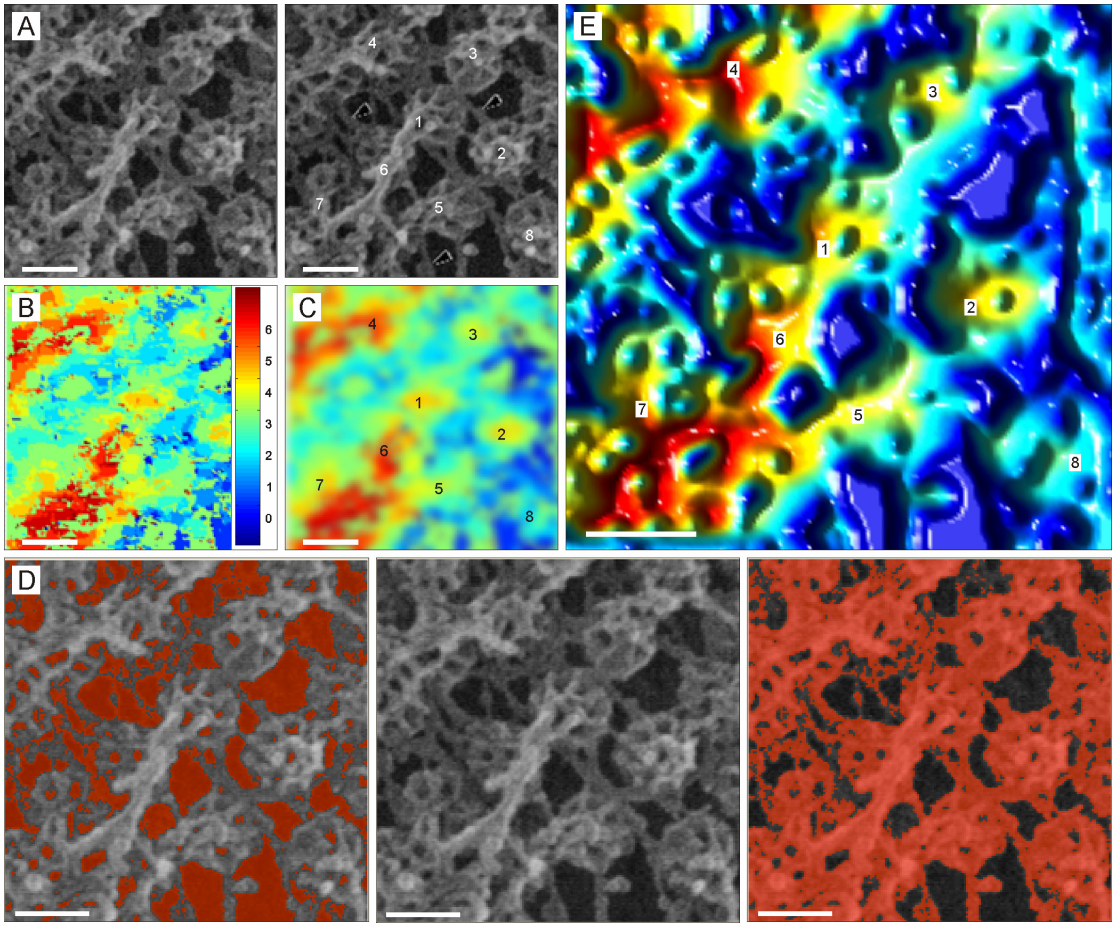

Figure 2.3.1 (**A**) Stereo pair of SE_1 FESEM images taken from Goldberg and Allen (1993) and presumed to be oriented approximately 7 degrees relative to one another. Numbers indicate the positions of individual nuclear pore baskets in the matching micrograph. (**B**) Disparity map calculated from x-differences in homologous point coordinates in left – and right images obtained by cross-correlation; colour-bar indicates the disparity (in pixels). A few of the points are obviously anomalous. (**C**) Disparity map from (B); median filtering was performed within a 3×3 neighbourhood (Matlab V6.5 The ©Mathworks Ltd.) and then Fourier filtered to 120Å resolution (Spider V9.05). The numbers indicate the positions of individual nuclear pore baskets. (D) The left-hand image (centre) was divided into regions of low (right) – and high (left) electron escape probability, masked regions are indicated in red. Because of the lack of topological information in areas of low electron escape probability, these were given an elevation of 0 and excluded from the reconstruction. (E) Final DEM, Fourier filtered to 120 Å resolution. Individual nuclear pore baskets can be distinguished (numbers); the resolution is insufficient to distinguish the morphology of individual nuclear pore baskets, however. The most elevated regions (indicated by red) lie above the most depressed (blue) by 600Å. Scale bar 100 nm.

Matching resulted in a large number of mismatches and the unfiltered disparity map (figure 2.3.1 B) is noisy; individual NPB can hardly be discerned. After median (3×3) and low-pass Gaussian filtering to 120 Å individual NPB become clearer, these are

labelled in figure 2.3.1 C. The approximate heights of individual NPB can be estimated from the disparity, but no details of individual NPB are visible (figure 2.3.1).

I reasoned that underexposed areas and areas of low electron escape probability (defined with a threshold intensity) should be removed from the reconstruction (figure 2.3.1 D). These areas were assigned a disparity of 0, the idea being that underexposed areas occur in holes or represent surfaces that lie further from the electron beam than the rest of the structure. They cannot contribute directly to the reconstruction, as they cannot be successfully matched. Removing them is equivalent to extracting the visual hull of the visible portion for a single viewpoint (figure 2.3.1 D, E).

The resulting DEM, low-pass Gaussian filtered to 120 Å is shown in figure 2.3.1 E). Some individual basket filaments can be discerned in the resulting reconstruction and the height of individual NPBs can be measured, but the resolution obtained is insufficient to resolve individual structures. However, despite being unsuitable for a structural description of the NPB, this low-resolution method could allow quantification of gross changes occurring as the result of perturbation experiments. As a comparison, an atomic force microscopy (AFM) perturbation experiment is shown in figure 2.3.2.

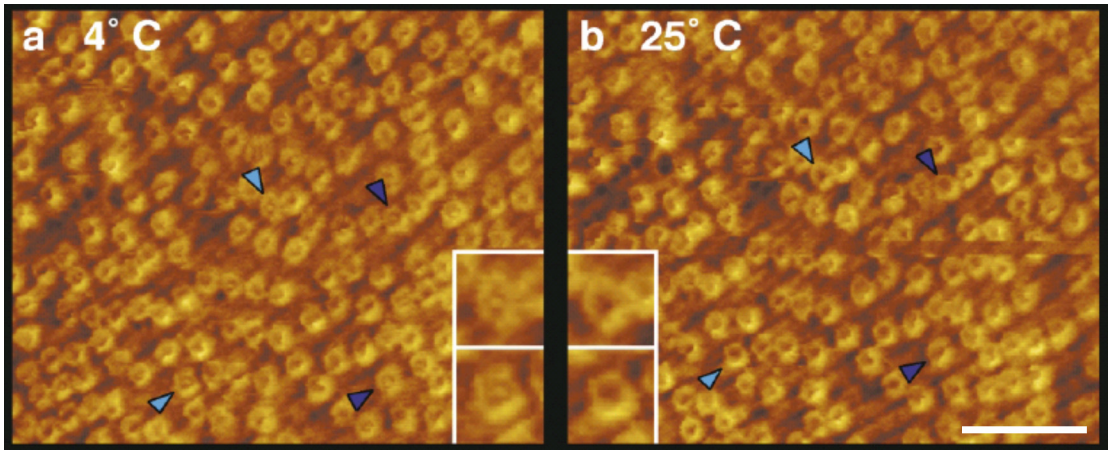

Figure 2.3.2 Individual NPB at 4°C and 25°C were imaged by AFM in contact mode. A greater percentage of the baskets at 4°C display a central plug/ transporter. The resolution is insufficient to visualise the basket filaments (from Stoffler *et al*., 2003). Scale bar: 500 nm. The topographic detail visible is inferior to the method shown here.

A second application of low-resolution imaging of the surface of the nucleoplasmic side of the nucleus, is to determine the position of individual pore baskets, three-dimensionally, in a lifelike context to determine the distribution of individual NPCs in the living cell.

A higher resolution reconstruction was produced from a higher magnification stereo-pair taken from Goldberg and Allen (1996) (figure 2.3.3 A). Individual basket filaments and distal ring are clearly visible in the unprocessed stereo micrographs (figure 2.3.3 A). The distal ring appears oval in shape and the distribution of pore filaments is not symmetric. The images were matched and the correlation coefficient matrix (figure 2.3.3 B) shows spuriously high correlations along the edges formed by areas of low electron escape probability and surrounding structure (figure 2.3.3 C). The nuclear membrane, although not underexposed, resulted in low correlation coefficients (figure 2.3.3 B), as the texture is not well resolved in the reference image (figure 2.3.3 A). The underexposed areas, largely occurring between individual basket filaments and ring, are indicated in figure 2.3.3 C, these were identified by thresholding. These areas were removed as in the first reconstruction, the resulting

DEM, after median and low-pass Gaussian filtering (120 Å) clearly shows the individual structures of the basket filaments and ring (figure 2.3.3 D).

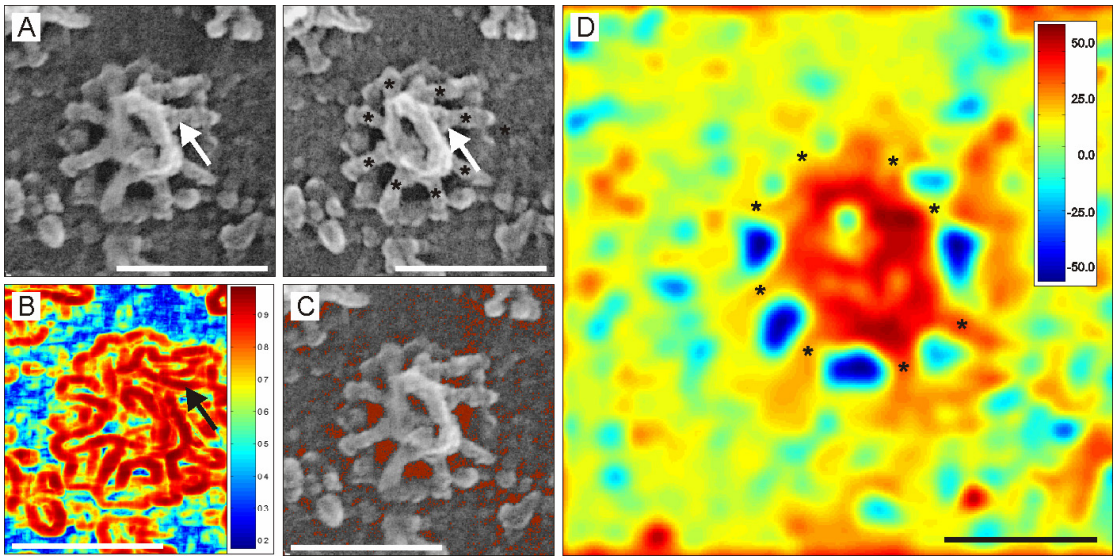

Figure 2.3.3. (**A**) Stereo FESEM micrograph of the nucleoplasmic side of a Xenopus oocyte nucleus. The image on the left is the reference – and the right hand image is the matching image. The arrow indicates one of the basket filaments. All eight of the filaments are indicated by stars (*) scale bar: 100 nm (B) The cross-correlation peak for every pixel in the reference image. The greatest peaks are found along the outer edges of the basket filaments and ring, where the intensity changes abruptly; these correlation coefficients are spuriously high and illustrate a shortcoming of the normalised correlation coefficient when large intensity differences are present. The surface of the nuclear membrane displays spuriously low correlations. Scale bar: 100 nm. (C) Areas of low electron escape probability do not contain sufficient contrast to be matched correctly and are therefore extracted from the disparity map. Because the number of electrons emitted from any point on the sample surface is proportional to the intensity of the resulting micrograph at that point, a threshold can be arbitrarily defined, below which too few electrons escape. Scale bar: 100 nm. (D) Final DEM filtered to 120 Å (12 nm) resolution, the elevation of the map is illustrated by colour, the most prominent part of the nuclear pore basket lies at an elevation of about 500Å (50nm). The basket filaments (*) and ring are clearly visible scale bar: 50 nm.

The filtered DEM was converted into a VRML model in Matlab v6.5 ©The Mathworks Inc. and imported into Chimera (Petterson *et al*., 2004). The resulting model can be rotated, sliced and measured. The NPB has distorted eight-fold symmetry. The distal ring is tilted by ~ 30º (figure 2.3.4 C) relative to the nuclear membrane. The diameter of the NPB is ~100 nm, individual basket filaments are ~ 60 nm long and the diameter of the ring is ~50 nm, the ring is held in position by the basket filaments ~50 nm above the surface of the membrane (figure 2.3.4), however, these measurements are ambiguous because the structure appears to have partially collapsed. These dimensions have been reported previously as ~120 nm diameter, 75

nm long basket filaments, 30 – to 60 nm distal ring (reviewed by Lim *et al*., 2006). But this disparity can be explained by shrinkage of the sample during preparation.

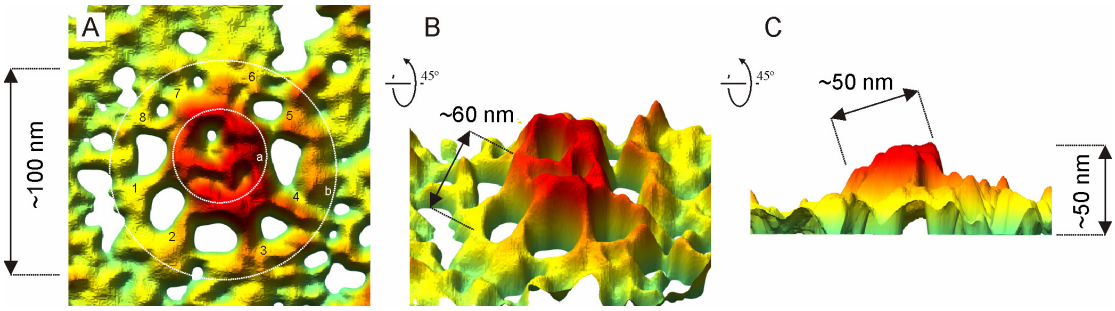

Figure 2.3.4. Analysis of the nuclear pore basket structure. (**A**) The ~100 nm nuclear pore basket viewed from above (b), the basket is comprised of eight irregularly arranged filaments (1-8) connected to a distal ring (a). (**B**) The same view as in (A) tilted by 45º as indicated. The basket filaments are ~60 nm in length. (**C**) The distal ring is tilted relative to the plane of the page by approximately 30º. The diameter of the distal ring is ~50 nm and it lies ~50 nm above the membrane surface.

2.4 Conclusions and future prospects

I have implemented a stereo matching algorithm in Matlab v6.5 ©The Mathworks and optimised it for FESEM stereo micrographs. Surface coordinates are triangulated using the methodology of Piazzesi (1973). A novel addition to the algorithm is the removal of areas with a low probability of electron escape, which is equivalent to a unidirectional silhouette intersection of the DEM. This greatly improves the quality of the resulting reconstruction. This method can be applied to any nearly continuous surface imaged by FESEM.

The ant did not have appropriate topology and did not present a nearly continuous surface and therefore the resulting reconstruction was of a rather poor quality. The nuclear pore basket reconstructions were more successful; the first reconstruction was of sufficient resolution for individual NPB to be identified from their structural signature alone. This could allow docking of higher resolution structures to produce a higher resolution model of the nuclear membrane. Large structural changes associated

with perturbation experiments might be observable at the available resolution which is comparable to that achieved by AFM.

The second reconstruction was of a higher resolution and allowed individual structural components to be measured and analysed. The ~50 nm diameter distal ring of the NPB protrudes ~50 nm above the membrane surface, maintained by ~60 nm basket filaments. The measured diameter of the entire complex is ~100 nm. These measurements are ~20 % smaller than previously reported, but this can be accounted for by shrinkage during fixation and dehydration. This shortcoming could possibly be overcome by rapid vitrification and freeze-drying followed by metal coating before examination in the FESEM. High-resolution micrographs, prepared in this way could provide valuable 3D structural information. At the highest possible FESEM resolution (20-40 Å) docking of atomic structures becomes a possibility. A method of docking volumetric data to 2½D DEMs is available (Dimmeler *et al*., 2001), which would allow atomic-resolution structures to be docked into low-resolution surfaces produced by the method described.

CHAPTER 3

VOLUMETRIC SEM RECONSTRUCTION

3.1 Introduction

Photogrammetric reconstruction methods have been successfully applied to FE/SEM micrographs (e.g. Hemmleb and Albertz, 1996) but these are severely limited by the topology generated. Stereoscopy (Piazzesi, 1973) and shape-from shading (Beil and Carlson, 1991) algorithms are the only techniques applied to the problem of three-dimensional (3D) reconstruction of biological samples viewed by FE/SEM. These methods constrain 3D shape to the digital elevation model (DEM), which consists of coordinates with associated elevations (reviewed by Ritter *et al*., 2004). These 2½ dimensional maps are not compatible with the majority of biological structure, such as "bent surfaces" (Lupetti *et al*., 2005) and this is a limitation shared with scanning tunnelling microscopy (STM) and atomic force microscopy (AFM), but in the case of AFM and STM the true topology is irrecoverable, while improved reconstruction methods could potentially recover the original topology of many objects that have been viewed using the SEM.

Samples that are prone to severe charging, those that lack sufficient texture, or consist of repeating structures cannot be reconstructed using existing stereoscopic techniques. In such cases matching fails and homologous points cannot be identified automatically (Cornille *et al*., 2003). Volumetric methods are capable of reconstructing an object in the presence of these artefacts (Eisert, 2001). Silhouette intersection methods in particular overcome many of the shortcomings associated with matching suboptimal SEM micrographs (Eisert, 2001; Slabaugh *et al*., 2001), these techniques result in a volume that approximates the visual hull, the maximal

shape that produces the same silhouette as the object for all views outside the convex hull (Laurentini, 1994). These methods are capable of reconstructing objects of arbitrary topology from several views of an object, obtained from different viewing directions.

The requirements for reconstructing the visual hull are:

1) That the silhouette of the object to be reconstructed can be extracted. This can be accomplished, rather laboriously by manually tracing the profile or by automated procedures, including thresholding
2) That the topology of the object is compatible with the visual hull reconstruction; concave surfaces are not reconstructed successfully
3) That the relative orientations of different views of the sample are known in each micrograph

No volumetric methods have been used to reconstruct FE/SEM data, despite the potential advantages of these methods when dealing with objects of arbitrary topology (such as biological samples). I have applied a probability-based silhouette-intersection reconstruction technique to a rotation series imaged in the scanning electron microscope. The volume was back-projected using the SIRT algorithm, implemented in Spider v9.05 (Frank *et al*., 1996).

3.2 Research design and methodology

An Argentine ant, *Linepithema humile* was killed by nitrogen asphyxiation and mounted onto the centre of a SEM specimen stub with a conductive carbon/ cryoprotectant mixture. The stub was cryo-plunged into slushy liquid nitrogen before

being freeze-dried at -90°C for two hours. After allowing the stub to reach room temperature, the sample was sputter coated with Gold-Palladium (Au-Pd) and transferred to a SEM (LEO S440, fitted with a LaB6 filament). The specimen was tilted so that the surface of the stub lay approximately perpendicular to the image plane and fifty micrographs (1024×768 pixels) were taken, representing a full rotation series with approximately seven degrees between micrographs.

The micrographs were aligned by finding peaks in a cross-correlation function (implemented in Matlab V6.5 ©Mathworks Ltd) between successive micrographs and windowed to 470×470 pixels. Every pixel in the windowed micrographs was associated with a probability of belonging to the set of background or foreground pixels. This was accomplished under the assumption that background and foreground pixel intensities are normally distributed; background and foreground pixel samples were manually sampled and the mean and standard deviation of the population estimated. The assignment of probability is illustrated in figure 3.2.1.

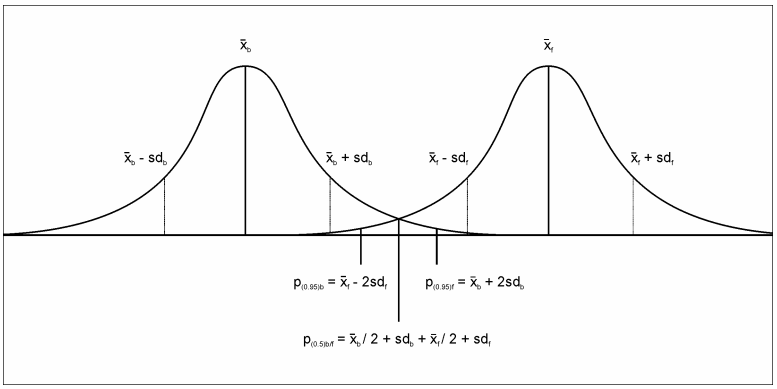

Figure 3.2.1. The foreground mean ($\bar{x}_f$) and standard deviation (sd_f) as well as the background mean ($\bar{x}_b$) and standard deviation (sd_b) are used to estimate a threshold range with associated probabilities ranging from ~ 0.02 to ~ 0.98 for a given pixel according to the Empirical Rule.

The assigned probabilities were placed in 470 × 470 matrices and assigned 8-bit grey scale intensities, illustrated in figure 3.2.2.

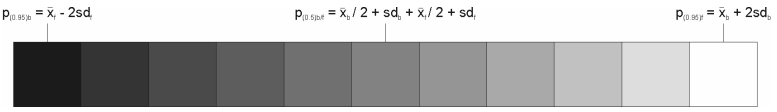

Figure 3.2.2. The probability matrix was assigned greyscale values of 0 to 255 for probabilities of belonging to the set of foreground pixels 0.02 to 0.98 respectively.

The resulting images were down-sampled to 100×100 pixels (bicubic interpolation) and imported into Spider v9.05. The simultaneous iterative reconstruction technique (SIRT) (Gilbert, 1972; Penczek *et al*., 1992; Penczek *et al*., 1997; Zhu *et al*., 1997) implemented in Spider was used to produce a back-projected voxel reconstruction with an angular increment of 7° between silhouette projections. The final volume, generated after optimisation of the SIRT parameters, was displayed using Chimera (Petterson *et al*., 2004).

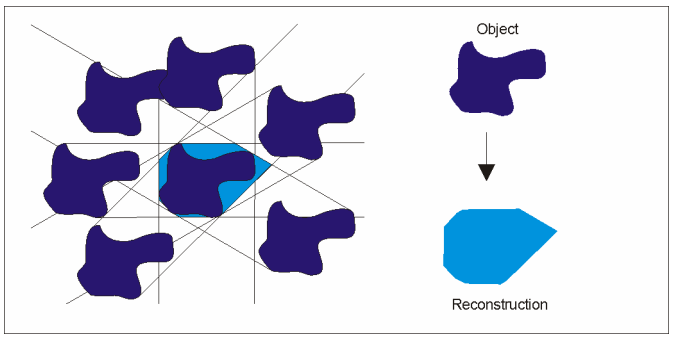

Figure 3.2.1. Illustration of the silhouette-intersection method of volumetric reconstruction. A cross-section through the object to be reconstructed is shown in dark blue. Multiple views are obtained of the object, the information possessed by the objects silhouettes are indicated by intersecting lines. These result in the (light blue) approximation of the visual-hull.

3.3 Results: presentation and discussion

Very little overlap of foreground – and background-pixel intensity was observed (figure 3.3.1). This aided silhouette thresholding, which in this case was successfully applied without user intervention, which can be time consuming if the number of micrographs is large.

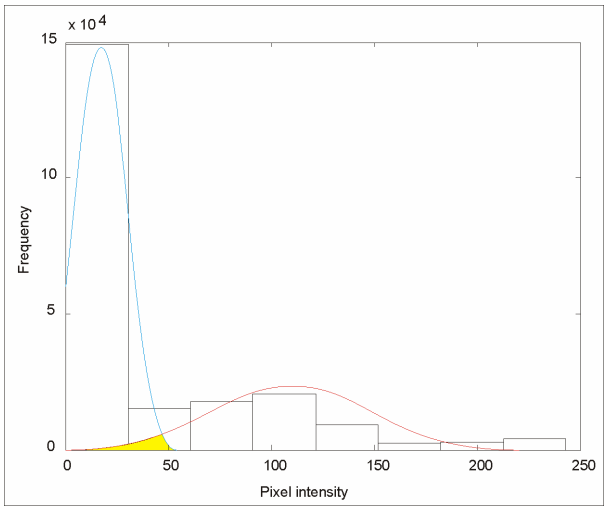

Figure 3.3.1 Pixel intensity histogram for the first micrograph of the rotation series. The background intensity is shown in blue and foreground, red. The overlapping region (shown in yellow) corresponding to ambiguously assigned pixels. These pixels were assigned grey-scale values as illustrated in figure 3.2.2.

The first five raw micrographs are shown in figure 3.3.2 A; each consecutive pair of images can be treated as a stereo pair and viewed by convergent or cross-eye stereo. The complete rotation series can thus be viewed in stereo, leading to a qualitative impression of 3D structure. To produce a 3D model, the images are segmented and back-projected. The effects of segmentation are shown in figure 3.3.2 B, the majority of pixels have been assigned a probability of 0.02 or 0.98 of belonging to the set of foreground pixels. These pixels have therefore been assigned grey-scale values of 0 or 255 respectively. These pixels are likely to be correctly classified, the intermediate pixels that occur in areas where the background is particularly light, such as above the antennae, or the foreground dark, such as the conductive paint at the base of the ant (figure 3.3.2 B) are assigned intermediate grey-scale intensities. After refinement of the SIRT parameters, a voxel model was generated (3.3.2 D). This map was contoured in Chimera (Petterson *et al.*, 2004) to enclose an arbitrary volume by comparison with the original micrographs (figure 3.3.2 E).

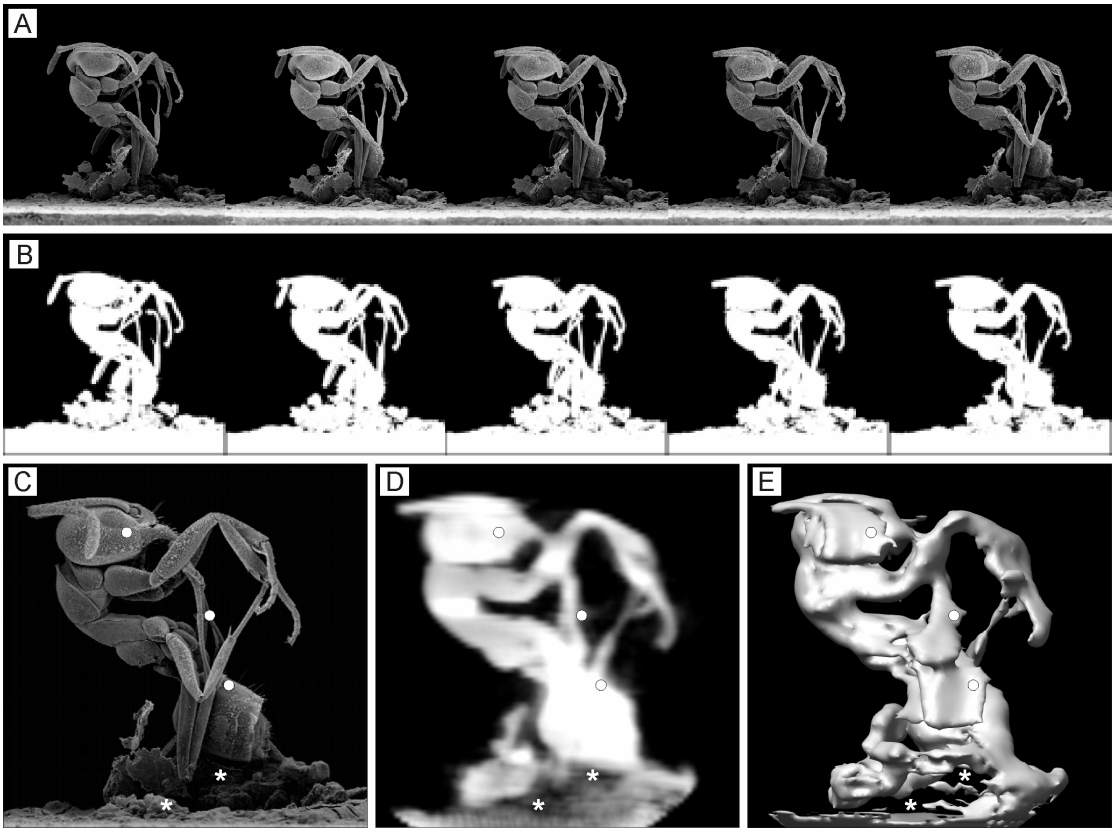

Figure 3.3.2 (**A**) The first five of a sample of fifty SEM images comprising a rotation series of a dehydrated, gold-palladium sputtered ant. The rotation axis is parallel to the plane of the page in the vertical direction and the angular increment between images is approximately seven degrees. (**B**) Images were segmented by thresholding; pixels considered to form part of the foreground were given a greyscale value of 255; those thought to be part of the background a value of 0, pixels lying in uncertain positions are given values between 0 and 255 depending on their proximity to the threshold value. (**C, D, E**) Comparison of an original image (C) with a voxel model derived from SIRT back-projection of fifty silhouetted images (D) and the result of meshing the voxel model by thresholding (E). Visual-hull artefacts, originating from structures not fully described by silhouettes are marked with circles (°) the internal detail of (C) is lost in silhouette (D) and results in anomalous structures (E). Thresholding errors resulting from areas near the thresholding value in the original images are indicated by stars (*) in (C) inducing anomalously dark volumes in the final reconstruction (shown by (*) in D), thresholding the voxel model relegates these dark volumes to the background shown by stars (*) in (E).

The SIRT algorithm was used to optimise a voxel model to correspond to what are essentially *probability-projections*. This is a robust method that allows some degree of error at the silhouette extraction stage as well as in relative micrograph orientations. This is an improvement over volume-intersection methods where a given voxel is discarded from the volume if it falls outside the silhouette in a single image (Eisert, 2001), which requires accurate segmentation of silhouettes and camera calibration and this means that the model does not always improve with an increase in the number of images used, and may become worse, as errors are additive (Liang and Wong, 2005).

Using the method described here, errors are averaged out, which means that an increase in views/ images leads to an improvement in the final reconstruction. This is an important consideration in the case of noisy FE/SEM micrographs that cannot be segmented accurately.

3.4 Conclusions and future prospects

I have applied the SIRT algorithm to silhouettes derived from SEM micrographs of an object possessing a complicated topology. This is the first application of silhouette intersection methods to the reconstruction an object from SEM micrographs. The reconstruction was successful within the limitations of the method. However, improvements could be made by:

1) Increasing the number of views, and having a more diverse range of orientations. This would reduce artefacts such as the extra density around the legs and antennae.
2) Improve thresholding, this would be most easily achieved by increasing the intensity difference between foreground – and background pixel intensities. This would reduce artefacts, such as the holes present around the conductive glue.
3) Improved orientation information, a more precise stage micrometer or applying calibration methods such as those described by Fusiello (2000). All attempts at iteratively improving initial angular assignments by projection-matching failed.
4) Refining the resulting mesh stereoscopically in order to improve resolution and allow concavities to be reconstructed.
5) Careful selection of samples that are adequately described by their visual hull.

Orthographic projection was assumed in the reconstruction although at the magnification utilised this assumption is not strictly correct. At low-magnification the angle of the scan-cone cannot be assumed to be negligible. Gnomonic projection therefore becomes significant at low magnification. This could lead to inconsistencies in the back projected map. At higher magnifications this projective geometry would closely approximate experimental conditions (Piazzesi, 1973). Highly charged objects can be segmented rather effectively by thresholding and the absence of tonal variation is not a limitation in the case of silhouette reconstruction. Samples could therefore be left uncoated and encouraged to charge in order to facilitate segmentation.

Stereoscopic refinement of the volumetrically-derived mesh is accomplished using pairs or triplets of images, which are matched in order to estimate surface coordinates. These together with those predicted from silhouette intersection are used to define an energy term which is minimised in order to determine the position of the final mesh. Concavities, which are not visible in silhouettes, and therefore cannot be reconstructed by silhouette-intersection, are available to stereoscopic algorithms. By combining these methods, a close approximation of the surface structure can be obtained (e.g. Esteban & Schmitt, 2004).

CHAPTER 4

METAL-SHADOWED TEM RECONSTRUCTION

4.1 Introduction

Cyanide hydratase (CHT) is a member of the nitrilase family of enzymes. Members of the family exhibit a broad range of specificities ranging from hydrogen cyanide to various aliphatic and aromatic nitriles (Pace and Brenner, 2001). In general, their natural substrates have not been identified. CHTs have been found in a variety of fungal species, but appear not to occur in bacteria or plants (Wang *et al*., 1999). They catalyse the conversion of cyanide to formamide with a small fraction (up to 0.4%, Nolan *et al*., 2003) being converted to formic acid. The different reaction pathways result from the breakage of a different bond in the tetrahedral thioimidate intermediate formed with the active site cysteine (reviewed by O'Reilly & Turner, 2003).

Gloeocercospora sorghi is a fungus that infects sorghum. When lesions are formed on sorghum, cyanoglycocides degrade to form hydrogen cyanide (HCN). Expression of CHT is induced in *G. sorghi* by HCN and this enzyme can account for up to 18% of the protein in the organism (Wang *et al*., 1992). It was therefore postulated that the purpose of the enzyme was to protect the pathogen in a high cyanide environment, however recent work (Wang *et al*, 1999) has shown that expression of CHT is not necessary for infectivity and thus its role in the cell remains uncertain. *G. sorghi* CHT has about 30% identity to the bacterial cyanide dihydratases (cynD) from *Pseudomonas stutzeri* AK61 and *Bacillus pumilus* C1. Both of these enzymes form self-terminating, homo-oligomeric spirals of 14 and 18 subunits respectively. The CHT from *G. sorghi* has a significantly higher molecular weight, (2-10 MDa) (Fry

and Millar, 1972), despite having a similar subunit molecular weight of ~40.9 kDa (Wang *et al*., 1992).

Because of the inherent enantiospecific nature and selectivity of enzymatic catalysis, nitrilases are used in a variety of industrial processes (Brady *et al*., 2004). An understanding of the structure of the nitrilase family would potentially lead to a rationalisation of the catalytic mechanism of these enzymes permitting rational design of nitrilases with altered characteristics. The Diversa Corporation has established a library of over 200 nitrilases identified and characterised by screening genomic libraries sampled from diverse environments (DeSantis *et al*., 2002). However, attempts to crystallize these have proved unsuccessful and no nitrilase crystal structure exists (DeSantis *et al*., 2002). The fungal cyanide hydratases occur as homo-oligomers or helices and spiral formation is thought to be necessary for activity (Nagasawa *et al*., 2000; Jandhyala *et al*., 2005), making quaternary structural studies of particular importance.

In this study we have demonstrated, for the first time, the effectiveness of applying IHRSR to frozen, partially dehydrated metal shadowed helices. The low-resolution structure of *G. sorghi* cyanide hydratase has been determined for the first time. We show here that the CH from *G. sorghi* forms extended left handed helices, built on similar principles to those described for the cyanide dihydratases (Sewell *et al*., 2005).

4.2 Research design and methodology

Margot Scheffer (Cape Town) expressed *G. sorghi* cyanide hydratase using recombinant clones obtained from Michael Benedik (Houston) as described by

Jandhyala (2005). Brandon Weber (Cape Town) purified the recombinant protein. Micrographs of unidirectionally shadowed sample were obtained on the Midilab instrument in the laboratory of Heinz Gross (Eidgenössische Technische Hochschule). Briefly, a drop of purified sample was pipetted onto glow-discharged, carbon-coated grids and allowed to absorb for two to three minutes before being rinsed in distilled water, blotted and rapidly vitrified by plunging into liquid nitrogen. Samples were cryo-transferred into the Midilab instrument, mounted onto a Philips-CM12 electron microscope, and freeze-dried for two hours at a temperature of 193 K (-80ºC) and pressure of 1027 mbar before being unidirectionally shadowed at 45º with 8 Å (0.8 nm) Tantalum/tungsten (Ta/W). Micrographs were recorded with a GATAN-794 Multiscan CCD camera at an electron dose of 0.5 to 1×10^3 e-/nm^2 at a magnification of 52 500× at a sampling of 5.3 Å/pixel.

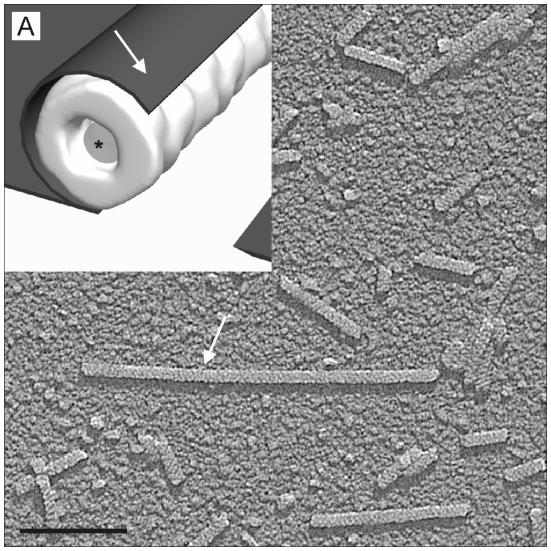

Figure 4.2.1. (**A**) Illustration of the metal-shadowing process, shadowing unidirectionally results in laterally asymmetrical micrographs. The majority of the metal falls onto the anterior surface of the helix resulting in disambiguation of the handedness of the helical symmetry. (**B**) Unprocessed micrograph of cryo-metal-shadowed *G. sorghi* nitrilase. The shadowing direction is indicated by an arrow and is at an elevation of 45º. The SNR of the micrograph is excellent and allows the handedness of the filament to be distinguished (left-handed) scale-bar indicates 100 nm.

Helical segments (1052) of 128×128 pixels with 96% overlap were selected and aligned using BOXER. The segments were band-pass filtered between 270 Å and 20

Å and normalised to a mean of 0 and standard deviation of 1. Boxed helical segments were aligned in a reference-free procedure and averaged in order to improve the SNR and the power spectrum was calculated (Figure 4.2.1.1A) using Spider V9.05.

4.2.1 helical symmetry determination

Horizontal intensity profiles were plotted across the three visible layer lines using Matlab V6.5 ©Mathworks Ltd (Figure 4.2.1.1A) and for each layer-line the distance between the meridional and layer-line maxima was measured. Bessel functions of the first kind, of order 1, 2, 3, 4 and 5 were plotted in Matlab V6.5 ©Mathworks Ltd (Figure 4.2.1.1B) the principal maxima are indicated. The ratio of the distance from each layer line to the meridional was calculated and compared to the ratios of the principal maxima of different Bessel orders. Figure 4.2.1.2 (table) shows the experimentally determined ratios compared to the theoretical ratios.

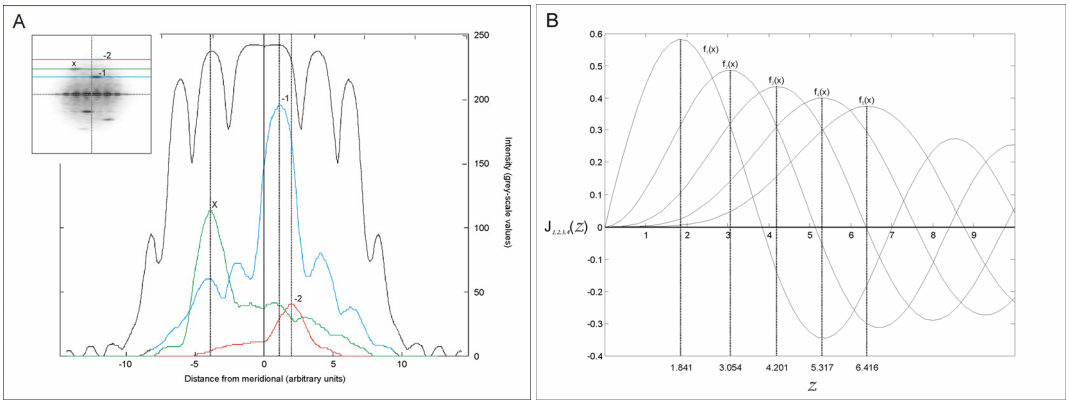

Figure 4.2.1.1 (**A**) (**inset**) Power spectrum calculated from the reference-free aligned helical segments. The coloured lines indicate where intensity profiles were obtained. (**Main**) Intensity profiles through the power spectrum, plotted in Matlab V.6.5 ©The Mathworks, Inc. The positions of the maxima are illustrated by dashed lines. (**B**) Bessel functions of the first kind, plotted in Matlab V.6.5 ©The Mathworks, Inc. Bessel functions of order 1,2,3,4 and 5 are plotted and the position of the first maxima indicated by dashed lines. The values are indicated.

Both of the indexing schemes match the data at the available resolution (figure 4.2.1.2). However, if the order of the unknown layer line is 4, an axial rise of 13 Å and 65º rotation per subunit is predicted, if on the other hand, the layer line is of order

5, the predicted helical parameters are an axial rise of 11 Å and 55º per subunit. Because these indexing schemes could not be distinguished by the power-spectrum of the raw data, IHRSR was applied starting from both of the predicted helical symmetries.

Ratio	Pred.	Meas.
1/2	0.603	0.558
1/3	0.438	
1/4	0.346	0.288
1/5	0.287	
2/3	0.727	
2/4	0.574	0.515
2/5	0.476	

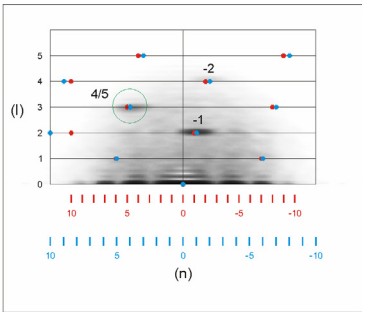

Figure 4.2.1.2 (**table**) the ratios of various maxima from Bessel functions of orders 1,2,3,4 and 5 (Pred.) are compared to the measured ratios (Meas.). The unknown spot is predicted to be of Bessel order 4 or 5. (**Figure**) The two indexing schemes are indistinguishable at the resolution available. Red spots indicate the resulting indexing scheme if the unknown spot is order 5, blue spots indicate the indexing scheme that results from the unknown spot being order 4. The pitch was predicted to be ~ 7 nm.

4.2.2 IHRSR

The IHRSR algorithm (Egelman, 2000) was initiated with blank cylinders, starting at the two helical symmetries predicted by indexing. The algorithm converged on two stable models, which approximated the symmetries predicted by the two alternate indexing schemes (Figure 4.2.1.3 A, B).

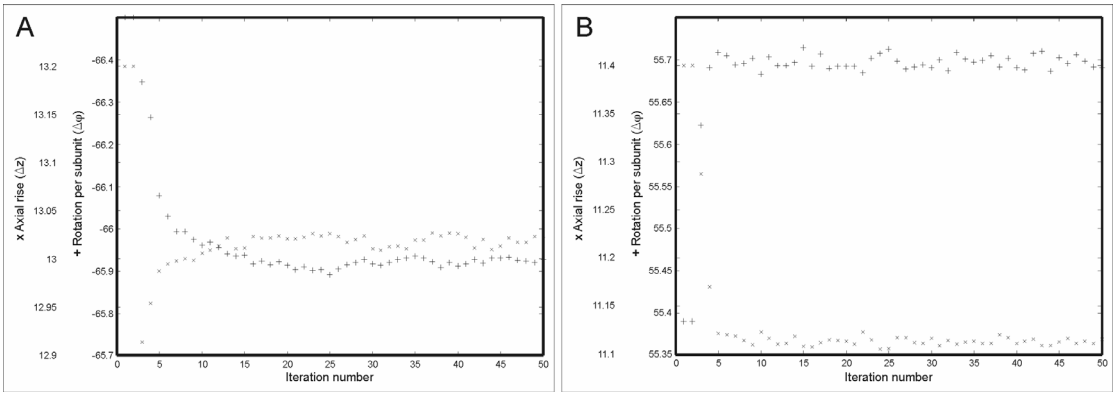

Fig. 4.2.1.3 Convergence of the IHRSR algorithm (Egelman, 2000). (**A**) The first indexing scheme predicted ~ 11 subunits per 2 rotations (11:2), the pitch was measured from the power spectrum to be ~7 nm and therefore with this indexing scheme, rotation per subunit (Δφ) was predicted to be ~65º and axial rise (Δz) was predicted to be ~13 Å. The final 25 iterations represent a convergence on a stable solution of Δφ = 65.921º ± 0.004º (95% confidence interval) and Δz = 13.019 Å ± 0.002 Å (95% confidence interval). (B) The second indexing scheme predicted ~13 subunits in 2 rotations (13:2), pitch = ~7nm predicts Δφ ≈ 55º and Δz ≈ 11 Å. And the IHRSR algorithm converged on a stable solution Δφ = 55.437º ± 0.004º (95% confidence interval) and Δz = 11.504 Å ± 0.001 Å (95% confidence interval). Statistics were calculated using Statistica 7.0 Statsoft Inc.

The reference-free aligned average of the boxed helical segments (figure 4.2.1.4 A) resemble the projection of the two models (figure 4.2.1.4 C, E) except that contrast arises from the anterior of the helix only, in the case of the reference free aligned average. The correct model cannot be distinguished, in this case, by comparing the data and model projections.

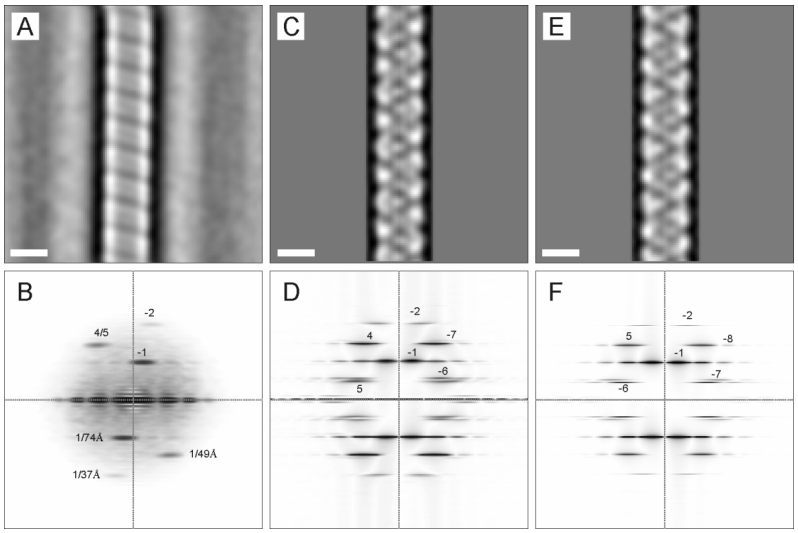

Fig. 4.2.1.4 (**A**) Averaged, reference-free aligned helical segments, the strong metal density is seen as black and the absence of metal as white. The left-handed one start helix, marked by diagonal striations is clearly visible. (**B**) Indexed power spectrum calculated from reference-free aligned helical segments; the layer-lines arise from the anterior surface of the helix only, and can be used to eliminate the ambiguity normally associated with helical projection. The layer-lines extend to approximately 1/37Å resolution. (**C**) Projection of the 11:2 model (resulting from assigning order 4 to the ambiguous layer-line). (**D**) Power spectrum generated from a single projection of the 11:2 model. The model power spectrum resembles the data power spectrum, except that layer lines 5 and -6 are not apparent in (B) and handedness ambiguity is present. (**E**) Projection of the 13:2 model (resulting from assigning order 5 to the ambiguous layer line). (**F**) Power spectrum generated from a single projection of the 13:2 model with the resulting indexing. Scale bar: 100 Å.

A greater number of layer-lines are apparent in the two model power-spectra than the data power spectrum, this can be explained by the improved quality of the model power spectra obtained by the imposition of helical symmetry. The correct model cannot be distinguished by comparing the model – and data power-spectra (figure 4.2.1.4 B, D, F). As predicted by superimposing the two indexing schemes (figure 4.2.1.2), the amplitudes of the layer-lines of the model power-spectra are indistinguishable (figure 4.2.1.4 D, F).

By including the phases into the power-spectrum, the correct model was identified. A 27 μm long helical segment was identified which displayed exceptional SNR. The two models were projected onto the centre of a 512×512 pixel image and aligned to the boxed raw helical segment. The Fourier transform was calculated for all three images and the phases and amplitudes were compared. The 11:2 helix matched the raw data in amplitude and phase, whereas the 13:2 helix only matched the amplitude (figure 4.2.1.5 A, B, C).

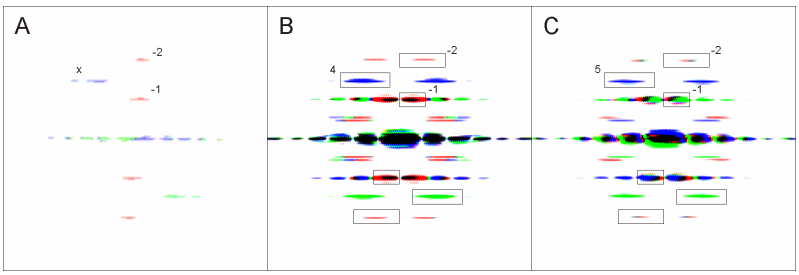

Fig. 4.2.1.5 (**A**) Computed Fourier transform from a single helical segment of 27 μm, the amplitudes of the Fourier transform are indicated by the intensity of colour, the phases are indicated by the hue. The layer-line orders are indicated. (**B**) The computed power spectrum from the aligned projection of the 11:2 model. The hue, and therefore the phases of the equivalent layer-lines are the same as (A). (**C**) The phases of the 13:2 model power-spectrum are not the same as (A).

The correct indexing scheme is therefore that of the 11:2 helix, as both the phases and amplitudes of the Fourier transform of the model agree with that of the raw data.

4.3 Results and discussion

4.3.1 unidirectional shadowing

Micrographs of unidirectionally shadowed material contain three-dimensional information in the form of surface normals. The thickness of the metal film deposited is directly related to the topology of the sample when viewed from a direction other than the original evaporation source (Gross, 1987). The resulting contrast is therefore

related to the surface topography in the resulting micrograph (Guckenberger, 1985). The unprocessed, unidirectionally shadowed micrographs of *G. sorghi* nitrilase reveal that the enzyme forms a filament with a mean length of 102 nm (standard deviation = 81 nm) with a maximum length of 528 nm and diameter of ~12 nm. The height of the fibre can be approximated from the length of the shadow cast by the fibre and the shadowing angle (figure 4.2.1 B). The height is approximately the same as the estimated diameter, suggesting that the fibre is not flattened. The prominent one-start left-handed helix is visible in unprocessed images (figure 4.2.1 B) and becomes clearer after reference-free averaging which improves the SNR of the images. Interestingly, a central channel can be seen in projection from this 2D average (figure 4.2.1.4 A).

4.3.2 Reconstruction

The IHRSR algorithm converged on a model that represents a metal cast of the outer envelope of the filament. In projection, this metal cast appears as a high-density hollow cylinder (black) surrounding a lower density filament (white) (figure 4.2.1.4 A, C); this is analogous to a negative-stain reconstruction. The filament was computationally extracted from the mould by thresholding to a volume corresponding to a subunit molecular mass of 45 KDa. The centre of the filament contains a narrow channel perforated with holes. The central channel and holes have been observed in previous reconstructions of helical and oligomeric nitrilases (Jandhyala *et al*., 2003; Sewell *et al*., 2003) and are believed to represent a feature of the nitrilase quaternary structure and not an artefact.

4.3.3 Symmetry of the model

The IHRSR algorithm converged on a model with an axial rise of ~13 Å and ~66° rotation per subunit (figure 4.2.1.3 A). The one-start helix has a pitch of 7.15 nm and there are 5.46 subunits per turn. The filament has a diameter of ~11.5 nm, a central channel of diameter ~6.2 nm. The filament has two dyad axes, which pass through sites of interaction homologous to those described in earlier reconstructions of helical and oligomeric nitrilases. The first passes through the A-surface, marked by a depression indicating the dimer interface and the hole. The second, lies through the D – and C-surfaces. The C-surface is the site at which adjacent dimers interact. The D-surface represents an interaction occurring across the one start helix, in this case occurring between dimers n and n+5. The helical symmetry is $D_1S_{\sim 5.48}$ (figure 4.3.3.1).

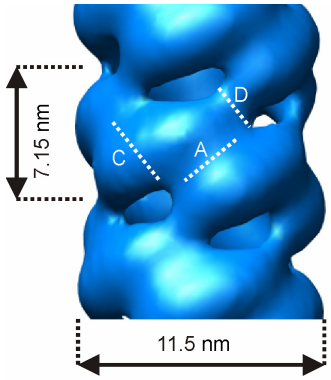

Figure 4.3.3.1 The filament; the protein core has been computationally extracted from the metal cast and contoured to a molecular mass of 45 KDa. The filament has a diameter of 11.5 nm and a pitch of 7.15 nm and has two dyad axes. The first dyad axis passes through the A-surface and the hole. The second lies through the D – and C-surfaces. The filament has a helical symmetry of $D_1S_{\sim 5.46}$.

4.3.4 Resolution

Edward H. Egelman kindly provided the protocol for resolution estimation by Fourier shell correlation (FSC). Briefly, two independent models were initialized with blank cylinders starting at different angles (φ_1 = -65.7°, φ_2 = -66.2°, $z_{1,2}$ = 13Å), the radial mask function was uncorrelated by using two different maximum helical diameters

(90Å and 93Å respectively). The two models were iterated fifty times and converged on the same stable solution. The two volumes were aligned in z and φ and windowed ($x_1 = 128$, $y_1 = 128$, $z_1 = 110$; $x_2 = 128$, $y_2 = 128$, $z_2 = 116$) and subsequently padded to the same volume (x = 128, y = 128, z = 128). The Fourier shell correlation was calculated between the two volumes with a ring size of 1 and plotted in Matlab V6.5 ©Mathworks Ltd, the FSC = 0.5 cut-off level is indicated (figure 4.3.3.2). The resolution was estimated to be ~33 Å.

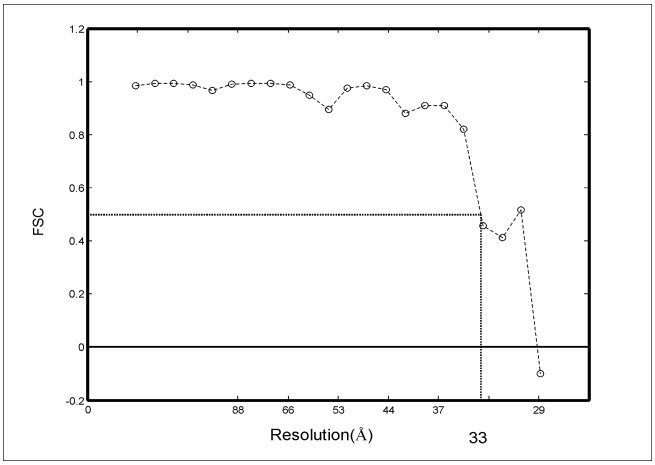

Figure 4.3.3.2 FSC resolution estimation. The resolution at the 0.5 cut-off level is 33 Å, similar to the resolution of highest resolution layer line in (figure 4.2.1.4 B) (37 Å).

Surface relief reconstruction (Guckenberger, 1985) provides a 2½ D digital elevation map of the structure of metal-shadowed surfaces. This method has been successfully applied (e.g. Rockel *et al*., 2000; Waltz *et al*., 1996; Dimmeler *et al*., 2001) to specimens of appropriate topology. However, the majority of biological structure is incompatible with the digital elevation map (Lupetti *et al*., 2005). The alternate method is to treat metal-shadowed surfaces as two-dimensional projections of the metal cast. Lanzavecchia *et al*. (1998) used the method of random conical tilt to reconstruct projections of metal replicas. Lanzavecchia *et al*. (2005) applied the method of conical-tilt tomography to metal-coated specimens of integral membrane

proteins. This method allows proteins to be studied, at high resolution, in the cellular milieu. Lupetti *et al*. (2005) applied a similar method to study dynein arms *in situ*.

4.4 Conclusions and future prospects

The ~33 Å helical structure of *G. sorghi* CHT has been determined by applying the IHRSR algorithm to freeze-dried unidirectionally shadowed filaments. The filaments have been unambiguously determined to be left-handed (Scheffer, 2006). Surfaces, where adjacent monomers bind were identified; these appear similar to those observed previously (Sewell *et al*., 2005). However, the resolution of the map was deemed insufficient for docking a homology model and therefore no hypothesis could be made about the residues involved in maintaining the stability of the helix. A higher resolution cryo-reconstruction would overcome this limitation, allowing rational design of crystallisable mutants by disrupting the various interacting surfaces and inhibiting spiral formation (Scheffer, 2006; Thuku, 2006). An understanding of the high-resolution structure of these enzymes would potentially lead to a rationalization of the catalytic mechanism, permitting rational design of nitrilases with altered characteristics.

The power-spectra of metal-shadowed helices resemble those obtained from negative-stain – and cryo-reconstructions; Fourier-Bessel helical reconstruction methods have been applied to metal-shadowed actin filaments (Morris *et al*., 1994). Single-particle methods have been applied to metal shadowed data (Lanzavecchia *et al*., 1998; 2005). In the present study, IHRSR was successfully applied to metal-shadowed filaments. This method has advantages over Fourier-Bessel methods in cases of Bessel overlap, inhomogeneity or when only short helical segments are available (Egelman, 2000;

Yang *et al*., 2003). IHRSR of metal shadowed specimens has a potentially wide range of applicability. A large proportion of the macromolecules in cells occur as helical structures, these include: actin, tubulin, myosin, RecA, Rad51, flagellin and pili (reviewed by Egelman, 2006). Application of the IHRSR algorithm to metal-shadowed freeze-dried, rapidly vitrified living cells would allow these structures to be viewed, in three dimensions in the context of the living cell. The resolution of these reconstructions would be in the range of ~20-30 Å (~2-3 nm), higher than currently possible with cryo-electron tomography (~4-5 nm) (reviewed by Baumeister, 2002).

CHAPTER 5

GENERAL DISCUSSION

5.1 Stereoscopic FESEM reconstruction

The majority of SEM stereoscopic algorithms have been developed for visualising the surfaces of non-biological, beam resistant samples (e.g. Stampfl *et al*., 1996; Scherer and Koledenik, 2001; Bony *et al*., 2005; Cornille *et al*., 2003). These micrograph stereo pairs are obtained under high-dose conditions at low magnification at accelerating voltages unsuitable for biological samples. Matching of the resulting micrographs is facilitated by the clear, textured images produced (e.g. Scherer and Koledenik, 2001). Recently, a project has been established between the Heinrich-Pette Institute and the Technical University of Berlin (e.g. Hemmleb and Schubert, 1997; Ritter *et al*., 2001; Ritter *et al*., 2003; Ritter *et al*., 2004) to develop a stereoscopic system capable of reconstructing high-resolution biological surfaces. Unfortunately the test samples analysed thus far consist of non-biological samples or low-magnification biological samples (e.g. Ritter *et al*., 2003).

I have implemented a stereoscopic algorithm based on those developed for beam resistant samples (e.g. Stampfl *et al*., 1996) and optimised it for high-magnification biological stereo FESEM micrographs. Biological samples lack sharp edges and corners useful in feature matching procedures (Hemmleb and Shubert, 1997) and near the resolving power of the microscope, blurring becomes apparent and the low dose necessary to reduce specimen damage and charging results in noise (Pawley, 1997). Despite these potential problems, cross-correlation based area matching was successfully applied. However, the resulting DEM is a low-resolution approximation of the topography of the sample. In order to improve the resolution of fine structures,

a novel background extraction step was incorporated into the algorithm. Areas of low electron escape probability, defined by a pixel intensity threshold, were assigned disparity values of zero. This has the effect of a unidirectional silhouette intersection, greatly improving the quality of the resulting DEM.

We believe that this is the first application of stereoscopic methods to biological macromolecular structure imaged by FESEM. The reconstruction from nuclear pore complex stereo pairs is encouraging; limited structural data such as linear dimensions could be extracted from the filtered and unidirectionally silhouetted 2½ dimensional DEM. The dimensions roughly conform to those obtained previously by a range of structural techniques, when correction is made for shrinkage during sample preparation. The greatest advantage of this method is that three-dimensional surface coordinates can be extracted without the need for averaging or symmetry imposition. The large magnification range available in the SEM allows correlative microscopy to be performed on a vast scale continuum from the organ – (cm) to the macromolecular (nm) scale. Combinations of structural data obtained from a variety of structural techniques need to be combined in order to understand the structure and mechanism of large cellular mechanisms, stereoscopic FESEM delivers structural data that is complementary to other structural methods.

5.2 Volumetric SEM reconstruction

The topological shortcomings of stereoscopic FESEM prompted us to apply a wider variety of photogrammetric reconstruction methods to the problem of SEM reconstruction. Full 3D models provide greater docking constraints and more complete structural description than surface relief – or DEM reconstructions

(Dimmeler *et al*., 2001): the failure to adequately describe the topology of the ant by the DEM illustrates this shortcoming. 3D object reconstruction from a series of 2D images is an old problem in the field of computer vision; many approaches have been devised, the oldest and possibly the simplest are silhouette intersection methods (Slabaugh *et al*., 2001). The advantage of silhouette intersection is that it can be applied successfully in the presence of common SEM artefacts such as charging or in situations where the object to be reconstructed lacks texture or is periodic, the SEM experimental set-up can be arranged to facilitate silhouette extraction.

The result is an approximation of the visual hull, which provides an estimate of the maximal volume of the object, guaranteed to exceed the volume of the reconstructed object. An increase in the number of viewing directions decreases the estimated volume monotonically (Slabaugh *et al*., 2001) however, unless the object lacks concavities, an infinite number of viewing directions still results in a volume greater than the original object. Concavities and structures not fully described by the available silhouettes therefore display artefactual density. This is clear of the ant reconstruction, where parts of the antennae and legs are surrounded by anomalous density. This situation can be improved by incorporating silhouettes derived from a greater variety of viewing directions. However, the inability of this method to reconstruct concavities is a fundamental limitation of this method, which cannot be improved by improving the number or quality of images.

In order to apply silhouette-intersection, images must be calibrated and silhouettes need to be extracted. Calibration is simplified by the assumption of parallel projection, which approximates the situation at high magnification in the SEM

(Piazzesi, 1973). Raw calibration data, obtained directly from the stage micrometer was used directly: after a refinement scheme, involving re-projection of the model failed. Although the SEM ant images could have been accurately calibrated relatively easily (Fusiello, 2000), it was envisioned that noisy and blurred images would present calibration difficulties. Therefore, silhouette intersection was performed in the face of poor calibration data, in an attempt to develop a sufficiently robust method capable of reconstruction in the presence of poor input data. Likewise silhouette extraction of noisy and blurry, high magnification FESEM micrographs of macromolecular complexes cannot be performed with certainty, a useful method must deal with this uncertainty.

I have applied the SIRT algorithm to a silhouetted, SEM-derived rotation series of an ant. In order to deal with silhouetting uncertainties, a threshold range, rather than a single value was used. Probabilities were assigned to each image pixel in the rotation series of belonging to the set of background or foreground pixels. The SIRT algorithm optimises the fit between the re-projection of the three-dimensional model and 2D input views (Gilbert, 1972; Penczek *et al*., 1992; Penczek *et al*., 1997; Zhu *et al*., 1997). This procedure results in a solution that is robust in the presence of inconsistencies resulting from noise and incorrect input orientations.

5.3 Metal-shadowed TEM reconstruction

Tomographic methods have now been applied successfully to rotationally-shadowed metal-coated macromolecular structures (Lanzavecchia *et al*., 1998; 2005; Lupetti *et al*., 2005). This method requires a completely different approach to that used for surface relief reconstruction (e.g. Rockel *et al*., 2000), rather than obtaining surface

normals and calculating a relief map, the metal density obtained by shadowing is treated as a projection and reconstructed by back-projection (Lanzavecchia *et al*., 1998). The result is a full 3D map of the metal cast, not constrained topologically by the DEM. The protein density is inferred from the negative-space contained by the cast (Lanzavecchia *et al*., 1998). This philosophy was applied to high-resolution unidirectionally shadowed helices obtained on the Midilab instrument in the laboratory of Heinz Gross, accomplished using the iterative helical real-space reconstruction (IHRSR) algorithm (Egelman, 2000).

The underlying assumption of both surface relief – and tomographic reconstruction is that single scattering can be assumed (Frank, 2006). This assumption cannot be taken for granted; multiple electron scattering events would break down the linear relationship between metal thickness and recorded intensity and lead to inconsistencies in the reconstruction. The probability of multiple scattering increases with metal-shadow thickness (Seal *et al*., 2006) and in this case, the metal coating is extremely fine. Furthermore, since the reconstruction was successful, it is reasonable to assume that the assumption: that this relationship is linear; is valid.

5.4 Identifying macromolecules in the cellular milieu

Cryo-electron tomography, the present method of choice for mapping macromolecules in the cellular context, results in 6-8 nm anisotropic resolution maps with poor SNR (Bohm *et al*., 2000). The resolution and SNR of a tomogram are dependent on the electron dose that a specimen can tolerate; this must be distributed over a wide angular tilt in order to fill Fourier space (e.g. Baumeister and Steven, 2000). One method of improving the SNR and/or resolution of a tomogram is by

freeze-substitution of heavy metal stain. This increases the tolerable dose and results in an improvement in SNR and close to life structural preservation at a resolution of ~6 nm (McIntosh, 2001). However, metal coating results in significantly better SNR and resolution: Lupetti *et al*. (2005) achieved a resolution of 2-3 nm (determined by FSC) and measured no electron damage after two hours of beam exposure to the metal cast.

Individual macromolecules crowd the cytoplasm (Grunewald *et al*., 2003) making it difficult to identify individual complexes. Cross-correlating a known macromolecular template in a tomographic volume represents a six dimensional search (Baumeister, 2005). This search-space is presently unfeasibly large when whole cells or organelles are considered: a small eukaryotic cell imaged at a resolution of ~6 nm generates 10^{10} bytes of data (McIntosh, 2001). Although strategies for decreasing the computational burden have been suggested, the problem remains largely unsolved (Bohm *et al*., 2000). This presents one of the obvious advantages of surface reconstruction: the search space for template matching is greatly decreased by several dimensions, depending on the search scenario. DEMs of preferentially oriented proteins, such as those exposed by freeze-fracture of vitrified membranes would require a three-dimensional search (two translations and one rotation) of a specially conceived template.

5.5 Conformational flexibility in the living cell

Many cellular processes rely on changes in protein conformation, for instance, a rotation between myosin domains results in a ~60 Å movement, which ultimately results in large-scale (cm) muscle contraction (Jontes and Milligan, 1997). Studies

that capture a snapshot of 3D macromolecular structure can elucidate the dynamics of macromolecular processes. An atomizer spray is used to deliver substrate, milliseconds before plunging, onto a grid; capturing macromolecules in various intermediate states. The particles are classified into discrete conformers, yielding structural –and kinetic data (reviewed by Saibil, 2000). These studies shed light on the dynamics and various conformational states of macromolecular machines; proteins and other cellular constituents. Alternatively; the structure of the macromolecule is determined before and after substrate addition (Jontes and Milligan, 1997). This provides a "before and after" view of the dynamic event.

Currently cryo-EM is the method of choice for characterising conformational states occurring in solution (Saibil, 2000). However, conducting these types of experiments on cell-surface macromolecular complexes, such as cell adhesion molecules, has certain advantages. No purification is necessary, which allows weakly interacting supramolecular structures, unable to withstand biochemical isolation (e.g. Bohm *et al*, 2000) to be viewed. Furthermore, analysis of metal-coated biological surfaces is unique in its ability to capture macromolecular structure at sufficient resolution and SNR for identifying and characterising individual macromolecular complexes without averaging or symmetry imposition. This allows the conformation of individual components of macromolecular complexes to be visualised without classification. Three-dimensional surface reconstruction has the potential to extend this capability, allowing quantitative analysis of conformers and docking of atomic resolution structures into reconstructions of different states.

5.3 Structural characterisation of macromolecular complexes

In order to solve the atomic-resolution structure of a protein by x-ray crystallography, high-quality macroscopic crystals are required. For some classes of proteins, this remains seemingly impossible. Microbial nitrilases are an excellent example of this (DeSantis *et al*., 2002). Furthermore, interactions between multiple subunits may not be preserved in the crystal lattice. In this case, individual components of the complex are purified and solved to atomic resolution by x-ray crystallography; the whole low resolution complex is solved by cryo-EM and individual components docked back into the EM-map (e.g. Adair and Yeager, 2002). Structural characterisation of the nuclear pore basket by FESEM has been accomplished descriptively already (e.g. Goldberg and Allen, 1996). Extending these types of studies to three-dimensions provides the possibility of docking, classification, statistical analysis and quantification of lengths and angles.

CHAPTER 6

CONCLUSIONS

6.1 Stereoscopic FESEM reconstruction

1) Stereoscopic reconstruction was applied to macromolecular stereo-images for the first time.

2) The low resolution 2.5 dimensional structure of the nuclear pore basket was determined

3) A novel method which consists of unidirectional silhouette extraction of low electron escape probability regions was implemented in order to improve the quality of stereoscopic disparity maps.

6.2 Volumetric SEM reconstruction

1) Volumetric reconstruction was applied to SEM micrographs for the first time.

2) A novel silhouette-intersection method was devised which utilizes the SIRT algorithm to optimize re-projected views of the volumetric model to the original silhouetted input views

3) To enable silhouetting uncertainties to be accounted for, a probability-based thresholding scheme was introduced so that artifacts, resulting from silhouetting errors were minimized.

6.4 Metal-shadowed TEM reconstruction

1) The low-resolution helical structure of a Microbial nitrilase from *Gloeocercospora sorghi* was determined.

2) The iterative helical real space reconstruction (IHRSR) technique was successfully applied to freeze-dried unidirectionally shadowed metal replicas for the first time.

3) We have demonstrated that metal shadowing reveals internal structural details; we propose this occurs through a process of metal atom internalization during the shadowing process.

REFERENCES

Adair, B.D. and Yeager, M. (2002). Three-dimensional model of the human platelet integrin αIIbβ3 based on electron cryomicroscopy and x-ray crystallography. *Proceedings of the National Academy of Sciences*, **99**(**22**): 14059-14064.

Aloy, P., böttcher, B., Ceulemans, H., Leutwein, C., Mellwig, C., Fischer, S., Gavin, A.C., Bork, P., Superti-Furga, G., Serrano, L. and Russell, R.B. (2004). Protein-based assembly of protein complexes in yeast. *Science*, **303**: 2026-2029.

Baumeister, W. (2002). Electron tomography: towards visualizing the molecular organization of the cytoplasm. *Current Opinion in Structural Biology*. **12**: 679-684.

Baumeister, W. (2005). From proteomic inventory to architecture. *FEBS Letters*, **579**: 933-937.

Baumeister, W. and Steven, A. (2000). Macromolecular electron microscopy in the era of structural genomics. *Trends in Biochemical Science*. **25**: 624-631.

Beck, M., Forster, F., Ecke, M., Plitzko, J.M., Melchior, F., Gerisch, G., Baumesiter, W. and Medalia, O. (2004). Nuclear pore complex structure and dynamics revealed by croelectron tomography. *Science*, **306**: 1387-1390.

Beil, W. and Carlsen, I.C. (1991). Surface reconstruction from stereoscopy and "shape form shading" in SEM images. *MVA 4*, 271-285.

Belhumeur, P.N. and Mumford, D. (1992). A Bayesian treatment of the stereo correspondence problem using half-occluded regions. *IEEE Conference on computer vision and pattern recognition*.

Bethal, W. and Bastacky, S.J. (1999). Measurement of Percieved Objects. *IEEE vis99 Proceedings.*

Bohm, J., Frangakis, A.S., Hegerl, R., Nickell, S., Typke, D. and Baumeister, W. (2000).Toward detecting and identifying macromolecules in a cellular context: Template matching applied to electron tomograms. *Proceedings of the National Academy of Sciences*. **97(26)**: 14245-14250.

Bony, A., Heid, A., Takakura, Y., Satzke, K. and Meyrueis, P. (2005). Waveguide sidewall roughness measurement on full wafers by SEM-based stereoscopy. *Journal of Microscopy*, **217(3)**: 188-192.

Brady, D., Beeton, A., Zeevaart, J., Kgaje, C., Van Rantwijk, F. and Sheldon, R.A. (2004). Characterisation of nitrilase and nitrile hydratase biocatalytic systems. *Applied Microbiology and Biotechnology*, **64**: 76-85.

Cazaux, J. (2005). Recent developments and new strategies in scanning electron microscopy. *Journal of Microscopy*, **217**(**1**): 16-35.

Cornille, N., Garcia, D., Sutton, M.A., McNeill, S.R. and Orteu, J.J. (2003). Automated 3-D reconstruction using a scanning electron microscope. *SEM Conference on Experimental and Applied Mechanics*, Charlotte, North Carolina, 2–4 June 2003.

Crowther, R.A. and Klug, A. (1975). Structural analysis of macromolecular assemblies by image reconstruction from electron micrographs. *Annual Review Biochemistry*, **44**: 161-182.

DeSantis G., Zhu, Z., Greenberg, W.A., Wong, K., Chaplin, J., Hanson, S.R., Farwell, B., Nicholson, L.W., Rand, C.L., Weiner, D.P., Robertson, D.E. and Burk, M.J. (2002). An enzyme library approach to biocatalysis: development of nitrilases for enantioselective production of carboxylic acid derivatives. *Journal of the American Chemical Society*, **124**: 9024-9025.

Dimmeler, E., Marabini, R., Tittman, P. and Gross, H. (2001). Correlation of topographic surface and volume data from three-dimensional electron microscopy. *Journal of Structural Biology*, **136**: 20-29.

Egelman, E.H. (2000). A robust algorithm for reconstruction of helical filaments using single-particle methods. *Ultramicroscopy*, **85**: 225-234.

Egelman, E.H. (2006). RecA assembly, one molecule at a time. *Structure*, **14**(**11**): 1600-1602.

Eisert, P. (2001). Reconstruction of volumetric 3D models. *3D Videocommunication* (Schreer, O., Kauff, P., Sikora, T., eds.) 133-150, Wiley Verlag, Berlin.

Erlandsen, S.L., Bitterman, A.G., White, J., Leith, A. and Marko, M. (2001). High-resolution cryo-FESEM of individual cell adhesion molecules (CAMs) in the glycocalyx of human platelets: detection of P-selectin (CD62P), GPI-IX complex (CD42a/CD42bα,bβ), and integrin GPIIbIIIa (CD41/CD61) by immunogold labelling and stereo imaging. *The Journal of Histochemistry and Cytochemistry*, **49(7)**: 809-819.

Esteban, C.H.A and Schmitt, F. (2004). Silhouette and stereo fusion for 3D object modelling. *Computer Vision and Image Understanding*, **96**(**3**): 367-392.

Frank, J.S. (1987). Membrane structure in ultrarapidly frozen, unpretreated, freeze-fractured myocardium. *Circulation research*, **61**: 141-147.

Frank, J. (2006). Three-dimensional electron microscopy of macromolecular assemblies. *Oxford University Press*, New York.

Frank, J., Radermacher, M., Penczek, P. Zhu, J., Li, Y., Ladjadj, M. and Leith, A. (1996). SPIDER and WEB: Processing and visualization of images in 3D electron microscopy and related fields. *Journal of Structural Biology,* **116**:190–199.

Frankot, R.T., Hensley, S. and Schafer, S. (1994). Noise resistant estimation techniques for SAR image registration and stereomatching. *International Geoscience*

and Remote Sensing Symposium, (IGARSS). Institute of Electrical and Electronic Engineers (IEEE), New York, 1151-1153.

Fry, W.E. and Millar, R.L. (1972). Cyanide degredation by an enzyme from *Stemphylium loti*. *Archives of Biochemistry and Biophysics*, **151**: 468-474.

Fuchs, K.H., Tittmann, P. and Gross, H. (1994). Cryo-microscopy and surface imaging of biological macromolecules. *ICEM 13-PARIS*, 23-24.

Fusiello, A. (2000). Uncalibrated Euclidean reconstruction: a review. *Image and Vision Computing*, **18**: 555-563.

Gallo, I. and Binaghi, E. (2005). A new algorithm for dense two-frame stereo correspondence. *VISAPP 2006: International Conference on Computer Vision Theory and Applications 2005.*

Garcia-Bustos, J.F., Wagner, P. and Hall, M.N. (1991). Yeast cell-free nuclear protein import requires ATP hydrolysis. *Experimental Cell Research*, **192**: 213-219.

Gilbert, H. (1972). Iterative methods for the three-dimensional reconstruction of an object from projections. *Journal of Theoretical Biology*, **36**: 105-117.

Goldberg, M.W., Cronshaw, J.M., Kiseleva, E. and Allen, T.D. (1999). Nuclear-pore-complex dynamics and transport in higher eukaryotes. *Protoplasma*, **209**(**3**/**4**): 144-156.

Goldberg, M.W. and Allen, T.D. (1993). The nuclear pore complex: three-dimensional surface structure revealed by field emission, in-lens scanning electron microscopy, with underlying structure uncovered by proteolysis. *Journal of Cell Science*, **106**: 261-274.

Goldberg, M.W. and Allen, T.D. (1996). The nuclear pore complex and lamina: three-dimensional structures and interactions determined by field emission in-lens scanning electron microscopy. *Journal of Molecular Biology*, **257**(**4**): 848-865.

Gross, H. (1987). High resolution metal replication of freeze-dried specimens. *Cryotechniques in Biological Electron Microscopy* (Steinbrecht, R.A. and Zierold, K., eds.) 205-215, Springer Verlag, Berlin.

Gross, H., Krusche, K. and Tittmann, P. (1990). Recent progress in high-resolution shadowing for biological transmission electron microscopy. *Proceedings of the XIIth International Congress for Electron Microscopy*, 510-511.

Grunewald, K., Medalia, O., Gross, A., Steven, A.C. and Baumeister, W. (2003). Prospects of electron cryotomography to visualize macromolecular complexes inside cellular compartments: implications of crowding. *Biophysical Chemistry*. **100**: 577-591.

Guckenberger, R. (1985). Surface reliefs derived from heavy-metal shadowed specimens: Fourier space technique applied to periodic objects. *Ultramicroscopy*, **16**: 357-370.

Hemmleb, M. and Albertz, J. (1996). Digital micophotogrammetry with the scanning electron microscope. *Commission V, Working Group 1*.

Hemmleb, M. and Schubert, M. (1997). Digital microphotogrammetry – determination of the topography of microstructures by scanning electron microscope. *Conference Proceedings of the Second Turkish-German Joint Geodetic Days*, 745-752.

Hermann, R. and Muller, M. (1997). Limits in high resolution scanning electron microscopy: natural surfaces? *Scanning*, **19**: 337-342.

Hoenger, A., Doerhoefer, M., Woehlke, G., Tittmann, P., Gross, H., Song, Y.H. and Mandelkow, E. (2000). Surface topography of microtubule walls decorated with monomeric and dimeric kinesin constructs. *Biological Chemistry*, **381**: 1001-1011.

Jandhyala, D., Berman, M., Meyers, P.R., Sewell, B.T., Willson, R.C. and Benedik, M.J. (2005). CynD, the cyanide dihydratase from *Bacillus pumilus*: gene cloning and structural studies. *Applied and Environmental Microbiology*, **69**(**8**): 4794-4805.

Jeffree, C.E., Rixon, H.W.M., Brown, G., Aitken, J. and Sugrue, R.J. (2003). Distribution of the attachment (G) glycoprotein and GM1 within the envelope of mature respiratory syncytial virus filaments revealed using field emission scanning electron microscopy. *Virology*, **306**: 254-267.

Jontes, J.D. and Milligan, R.A. (1997). Brush border myosin-I structure and ADP-dependent conformational changes revealed by cryoelectron microscopy and image analysis. *Journal of Cell Biology*, **139**(**3**): 683-693.

Kammerud, C., Abidi, B., Huq, S. and Abidi, M. (2005). 3D nanovision for the inspection of micro-electro-mechanical systems. *IEEE International Conference on Electronics, Circuits, and Systems*.

Lanzavecchia, S., Bellon, P.L., Lupetti, P., Dallai, R., Rappuoli, R. and Telford, J.L. (1998). Three-dimensional reconstruction of metal replicas of the *Helicobacter pylori* vacuolating cytotoxin. *Journal of Structural Biology*, **121**: 9-18.

Lanzavecchia, S., Cantele, F., Bellon, P.L., Zampighi, L., Kreman, M., Wright, E. and Zampighi, G.A. (2005). Conical tomography of freeze-fracture replicas: a method for the study of integral membrane proteins inserted in phospholipid bilayers. *Journal of Structural Biology*, **149**: 87-98.

Laurentini, A. (1994). The visual hull concept for silhouette-based image understanding. *Pattern Analysis and Machine Intelligence*, **16**(**2**): 150-162.

Liang, C. and Wong, K.Y.K. (2005). Complex 3D shape recovery using a dual-space approach. *IEEE Computer Society,* International Conference on Computer Vision and Pattern Recognition.

Lim, R.Y.H., Aebi, U. and Stoffler, D. (2006). From the trap to the basket: getting to the bottom of the nuclear pore complex. *Chromosoma*, **115**: 15-26.

Lucas, B.D. and Kanade, T. (1981). An iterative image registration technique with an application to stereo vision. *Proceedings of Imaging Understanding Workshop,* 121-130.

Lupetti, P., Lanzavecchia, S., Mercati, D., Cantele, F., Dallai, R. and Mencarelli, C. (2005). Three-dimensional reconstruction of axonemal outer dynein arms *in situ* by electron tomography. *Cell Motility and the Cytoskeleton*, **62**: 69-83.

Marko, M. and Leith, A. (1996). Stereocon-three dimensional reconstructions from stereoscopic contouring. *Journal of Structural Biology*, **116**: 93-98.

Matsuoka, K., Schekman, R., Orci, L. and Heuser, J.E. (2001). Surface structure of the COPII-coated vesicle. *Proceedings of the National Academy of Sciences*, **98**: 13705-13709.

McIntosh, J.R. (2001). Electron microscopy of cells: a new beginning for a new century. *The Journal of Cell Biology*, **153**: f26-f32.

Medalia, O., Weber, I., Frangakis, A.S., Nicastro, D., Gerisch, G. and Baumeister, W. (2002). Macromolecular architecture in eukaryotic cells visualized by cryoelectron tomography. *Science*, **298**: 1209-1213.

Morris, E.P., Katayama, E. and Squire, J.M. (1994). Evaluation of high-resolution shadowing applied to freeze-fractured, deep-etched particles: 3D helical reconstruction of shadowed actin filaments. *Journal of Structural Biology*, **113**: 47-55.

Mullins, R.D., Heuser, J.E. and Pollard, T.D. (1998). The interaction of Arp2/3 complex with actin: nucleation, high affinity pointed end capping, and formation of branching networks of filaments. *Cell Biology*, **95**: 6181-6186.

Nagasawa, T., Wieser, M., Nakamura, T., Iwahara, H., Yoshida, T. and Gekko, K. (2000). Nitrilase of Rhodococcus rhodochrous J1: conversion into the active form by subunit association. *European Journal of Biochemistry*, **267**, 138-144.

Nolan, L.M., Harnedy, P.A., Turner, P., Hearne, A.B. and O'Reilly, C. (2003). The cyanide hydratase enzyme of *Fusarium lateritium* also has nitrilase activity. *FEMS Microbiology Letters*, **221**: 161-165.

O'Reilly, C. and Turner, P.D. (2003). The nitrilase family of CN hydrolysing enzymes – a comparative study. *The Society for Applied Microbiology*, **95**: 1161-1174.

Pace, H.C. and Brenner, C. (2001). The nitrilase superfamily: classification, structure and function. *Genome Biology*, **2**(**1**): reviews0001.1-0001.9.

Pante, N. and Kann, M. (2002). Nuclear pore complex is able to transport macromolecules with diameters ~39 nm. *Molecular Biology of the Cell*, **13**: 425-434.

Pawley, J. (1997). The development of field-emission scanning electron microscopy for imaging biological surfaces. *Scanning*, **19**: 324-336.

Penczek, P., Radermacher, M. and Frank, J. (1992). Three-dimensional reconstruction of single particles embedded in ice. *Ultramicroscopy*, **40**: 33-53.

Penczek, P.A., Zhu, J., Schröder, R and Frank, J. (1997). Three-dimensional reconstruction with contrast transfer function compensation from defocus series. *Scanning Microscopy Supplement*, **11**: 1-10.

Peters, R. (1986). Fluorescence microphotolysis to measure nucleocytoplasmic transport and intracellular mobility. *Biochimica et Biophysica Acta*, **864**:305-359.

Pettersen, E.F., Goddard, T.D., Huang, C.C., Couch, G.S., Greenblatt, D.M., Meng, E.C., and Ferrin, T.E. (2004). "UCSF Chimera - A Visualization System for Exploratory Research and Analysis." *Journal of Computational Chemistry,* **25**: 1605-1612.

Piazzesi, G. (1973). Photogrammetry with the scanning electron microscope. *Journal of Physics E: Scientific Instruments*, **6**: 392-396.

Richards, R.G., Owen, G.Rh. and Gwynn, I.ap. (1999). Low voltage backscattered imaging (<5kV) using field emission scanning electron microscopy. *Scanning Microscopy*, **13(1)**: 55-60.

Richardson, W.D., Mills, A.D., Dilworth, S.M., Laskey, R.A. and Dingwall, C. (1988). Nuclear protein migration involves two steps: rapid binding at the nuclear envelope followed by slower translocation through nuclear pores. *Cell*, **52**: 655-664.

Ris, H. (1989). Three-dimensional imaging of cell ultrastructure with high resolution low voltage SEM. *Inst Phys Conf Ser*, **98**: 657–662.

Ritter, M., Hemmleb, M., Sinram, O., Albertz, J. and Hohenberg, H. (2004). A versatile 3D calibration object for various micro-range measurement methods. *ISPRS XXth Congress, Istanbul, Turkey, Volume XXXV, Part B, Commision* **5**: 696-701.

Ritter, M., Sinram, M., Hemmleb, H., Kleindiek, S., Schertel, A. and Honenberg, H. (2001). Photogrammetric reconstruction of biological surfaces on the basis of scanning electron microscope (SEM) data (poster). *3-Landertagung fur electronenmikroskopie Innsbruck.*

Ritter, M., Sinram, O., Albertz, J. and Honenberg, H. (2003). Quantitative 3D reconstruction of biological surfaces (abstract). *Microscopy and Microanalysis*, **9(3)**: 476-477.

Rockel, B., Guckenberger, R., Gross, H., Tittmann, P. and Baumeister, W. (2000). Rotary and unidirectional metal shadowing of VAT: localization of the substrate-binding domain. *Journal of Structural Biology*, **132**: 162-168.

Saibil, H.R. (2000). Conformational changes studied by cryo-electron microscopy. *Nature Structural Biology*, **7**(**9**): 711-714.

Scheffer, M.P. (2006). Helical structures of the cyanide degrading enzymes from *Gloeocercospora sorghi* and *Bacillus pumilus* providing insights into nitilase quaternary interactions. *MSc minithesis, University of the Western Cape*.

Scherer, S. and Kolednik, O. (2001). A new system for automatic surface analysis in SEM. *Microscopy and Analysis*, **70**:15-17.

Seal, K., Genov, D.A., Sarychev, A.K., Noh, H., Shalaev, V.M., Ying, Z.C., Zhang, X. and Cao, H. (2006). Coexistence of localised and delocalised surface plasmon modes in percolating metal films. *Physical review letters*, **97**: 2061031-4.

Sewell, B.T., Thuku, R.N., Zhang, X. and Benedik, M.J. (2005). Oligomeric structure of nitrilases: effect of mutating interfacial residues on activity. *Annals of the New York Academy of Sciences*, **1056**: 153-159.

Slabaugh, G., Culbertson, B., Malzbender, T. and Schafer, R. (2001). A survey of methods for volumetric scene reconstruction from photographs. *International Workshop on Volume Graphics.*

Smith, P.R. and Kistler, J. (1977). Surface reliefs computed from electron micrographs of heavy metal shadowed specimens. *Journal of Ultrastructure Research*, **61**: 124-133.

Southworth, D., Strout, G. and Russel, S.D. (1997). Freeze-fracture of sperm of Plumbago zeylanica l. in pollen. *Sexual Plant Reproduction*, **10**: 217-226.

Stampfl, J., Scherer, S., Gruber, M. and Kolednik, O. (1996). Reconstruction of surface topographies by scanning electron microscopy for application in fracture research. *Applied Physics A*, **63**: 341-346.

Stampfl, J., Wob, A., Kolednik, O. and Fratzl, P. (2002). Object reconstruction and object construction: applications in materials science. *Recent Research Developments in Applied Physics*, **5**: 89-106.

Stockroos, I., Kalicharan, D., Van Der Want, J.J.L. and Jongebloed, W.L. (1998). A comparative study of thin coatings of Au/Pd, Pt and Cr produced by magnetron sputtering for FE-SEM. *Journal of Microscopy*, **189**: 79-89.

Stoffler, D., Feja, B., Fahrenkrog, B., Walz, J., Typke, D. and Aebi, U. (2003). Cryo-electron tomography provides novel insights into nuclear pore architecture: implications for nucleocytoplasmic transport. *Journal of Molecular Biology*, **328**: 119-130.

Thuku, R.N. (2006). The structure of the nitrilase from Rhodococcus rhodochrous J1: homology modelling and three-dimensional reconstruction. *MSc minithesis, University of the Western Cape.*

Vasu, S.K. and Forbes, D.J. (2001). Nuclear pores and nuclear assembly. *Current Opinion in Cell Biology*, **13**: 363-375.

Volkmann, N., Amann, K.J., McPhie, S.S., Egile, C., Winter, D.C., Hazelwood, L., Heuser, J.E., Li, R., Pollard, T.D. and Hanein, D. (2001). Structure of Arp2/3 complex in its activated state and in actin filament branch junctions. *Science*, **293**: 2456-2459.

Walther, P. and Muller, M. (1997). Double layer coating for field emission cryo scanning electron microscopy – present state and applications. *Scanning*, **19**: 343-348.

Walz, T., Tittmann, P., Fuchs, K.H., Müller, D.J., Smith, B.L., Agre, P., Gross, H. and Engel, A. (1996). Surface topographies at subnanometer-resolution reveal asymmetry and sidedness of aquaporin-1. *Journal of Molecular Biology*, **264**: 907-918.

Wang, P., Matthews, D.E. and Van Etten, H.D. (1992). Purification and characterization of cyanide hydratase from the phytopathogenic fungus Gloeocercospora sorghi. *Archives of Biochemistry and Biophysics*, **298**(**2**): 569-575.

Wang, P., Sandrock, R.W. and VanEtten, H.D. (1999). Disruption of the cyanide hydratase gene in *Gloeocercospora sorghi* increases its sensitivity to phytoanticipin cyanide but does not affect its pathogenicity on the cyanogenic plant sorghum. *Fungal Genetics and Biology*, **00**: 126-134.

Wente, S.R. (2000). Gatekeepers of the nucleus. *Science*, **288**: 1374-1377.

Yang, Q., Rout, M.P. and Akey, C. (1998). Three-dimensional architecture of the isolated yeast nuclear pore complex: function and evolutionary implications. *Molecular Cell*, **1**: 223-234.

Yang, S., Yu, X., Galkin, V.E. and Egelman, E.H. (2003). Issues of resolution and polymorphism in single-particle reconstruction. *Journal of Structural Biology*, **144**: 162-171.

Zhu, J., Penczek, P.A., Schröder, R. and Frank, J. (1997). Three-dimensional reconstruction with contrast transfer function correction from energy-filtered cryoelectron micrographs: procedure and application to the 70S Escherichia coli ribosome. *Journal of Structural Biology*, **118**: 197-219.